

# Bidirectional Cross-Attention Fusion of High-Res RGB and Low-Res HSI for Multimodal Automated Waste Sorting

Jonas V. Funk<sup>a,b,\*</sup>, Lukas Roming<sup>b</sup>, Andreas Michel<sup>b</sup>, Paul Bäcker<sup>b</sup>, Georg Maier<sup>b</sup>, Thomas Längle<sup>a,b</sup>, Markus Klute<sup>a</sup>

<sup>a</sup>*KIT, Karlsruhe Institute of Technology, 76131 Karlsruhe, Germany*

<sup>b</sup>*Fraunhofer IOSB, Fraunhofer Institute of Optronics, System Technologies and Image Exploitation, 76131 Karlsruhe, Germany*

---

## Abstract

Growing waste streams and the transition to a circular economy require efficient automated waste sorting. In industrial settings, materials move on fast conveyor belts, where reliable identification and ejection demand pixel-accurate segmentation. RGB imaging delivers high-resolution spatial detail, which is essential for accurate segmentation, but it confuses materials that look similar in the visible spectrum. Hyperspectral imaging (HSI) provides spectral signatures that separate such materials, yet its lower spatial resolution limits detail. Effective waste sorting therefore needs methods that fuse both modalities to exploit their complementary strengths. We present Bidirectional Cross-Attention Fusion (BCAF), which aligns high-resolution RGB with low-resolution HSI at their native grids via localized, bidirectional cross-attention, avoiding pre-upsampling or early spectral collapse. BCAF uses two independent backbones: a standard Swin Transformer for RGB and an HSI-adapted Swin backbone that preserves spectral structure through 3D tokenization with spectral self-attention. We also analyze trade-offs between RGB input resolution and the number of HSI spectral slices. Although our evaluation targets RGB-HSI fusion, BCAF is modality-agnostic and applies to co-registered RGB with lower-resolution, high-channel auxiliary sensors. On the benchmark SpectralWaste dataset, BCAF achieves state-of-the-art performance of 76.4% mIoU at 31 images/s and 75.4% mIoU at 55 images/s. We further evaluate a novel industrial dataset: K3I-Cycling (first RGB subset already released on Fordatis). On this dataset, BCAF reaches 62.3% mIoU for material segmentation (paper, metal, plastic, etc.) and 66.2% mIoU for plastic-type segmentation (PET, PP, HDPE, LDPE, PS, etc.).

**Keywords:** Multi-modal fusion, Sensor-based sorting, Polymer identification, Near-Infrared (NIR), Short-Wave Infrared (SWIR), Packaging waste

---

## 1. Introduction

The transition towards a circular economy requires high-quality sorting of heterogeneous waste streams by material to enable efficient recycling. Automated waste sorting plants address this need using sensor-based sorting systems comprising high-throughput conveyor belts, where objects must be detected and ejected with compressed air nozzles. This setting demands reliable, real-time, pixel-level semantic segmentation that can cope with clutter, occlusions, contamination, and variable object appearances [1].

A range of sensors is deployed for such sorting tasks. RGB cameras capture color, texture, and shape cues. Hyperspectral imaging (HSI) in the near-infrared

(NIR, ~700-1000 nm) and short-wave infrared (SWIR, ~1000-2500 nm) ranges supports material identification. Other application-specific sensors include X-ray transmission, fluorescence systems, laser-induced breakdown spectroscopy (LIBS), and Raman spectroscopy. For polymer sorting in particular, HSI exploits characteristic absorption features to discriminate polyethylene terephthalate (PET), polyethylene (PE), polypropylene (PP), and other polymers [2, 3].

Previous work has shown that segmentation performance can often be improved by fusing heterogeneous sensors [4, 5, 6, 7]. In this article, we follow this direction by fusing RGB and HSI: RGB excels at high-resolution spatial detail but cannot reliably separate materials with similar colors, whereas HSI provides the

spectral richness needed for material discrimination but sacrifices spatial resolution. We argue that exploiting the strengths of both modalities without collapsing spectral information or eroding spatial detail is a promising approach for improved semantic waste segmentation on conveyor belts, and it motivates fusion mechanisms that respect each modality’s native resolution and structure while remaining efficient enough for deployment on commodity hardware.

To address this, we introduce Bidirectional Cross-Attention Fusion (BCAF), a multimodal architecture that fuses RGB and HSI without sacrificing either modality’s native strengths. BCAF aligns modalities at their native resolutions across multiple scales via localized bidirectional cross-attention between fine-grid RGB features and coarse-grid multi-slice HSI features. The HSI pathway preserves spectral information, while the RGB pathway retains high-resolution spatial context. Both backbones build upon hierarchical Swin Transformer encoders [8]. We additionally construct unimodal RGB and HSI segmentation pipelines based on these backbones paired with a shared U-Net-like decoder [9] and compare them against BCAF.

This native-resolution, channel-preserving fusion setting represents a broader class of multimodal systems that combine high-resolution RGB with lower-resolution, high-channel auxiliary sensors. Such configurations are common because silicon CMOS processes enable inexpensive, high-resolution RGB cameras, whereas hyperspectral and other non-RGB sensors still require more complex materials and fabrication, which limits their attainable resolution. We therefore expect BCAF to transfer to other RGB+X sensor combinations of this kind.

We evaluate our method on two datasets: SpectralWaste [10] and a novel dataset called K3I-Cycling. We consider two tasks: material-type segmentation (paper, metal, plastic, etc.) and plastic-type segmentation (PET, PP, HDPE, LDPE, PS, etc.), targeting the increasing recycling requirements for packaging waste set by, for example, the European Union [11].

Our study yields five main findings: (i) for both evaluated datasets, increasing RGB input resolution (256  $\rightarrow$  512  $\rightarrow$  1024) improves Swin-based semantic segmentation, (ii) preserving native high-resolution RGB detail (*resolution as information*) yields gains beyond scaling alone, (iii) the optimal number of HSI spectral slices depends on task granularity: material segmentation peaks with fewer slices, whereas fine-grained plastic-type segmentation benefits from more slices to capture subtle spectral cues, (iv) the adapted HSI backbone preserves more discriminative spectral information than an HSI-

to-RGB band-projection baseline using an RGB backbone, and (v) BCAF consistently outperforms unimodal baselines and learned-logit late fusion, achieving real-time throughput. In summary, BCAF achieves state-of-the-art semantic segmentation on SpectralWaste with 76.4% mIoU at 31 images/s and 75.4% mIoU at 55 images/s on an NVIDIA GeForce RTX 4090. On the novel K3I-Cycling dataset, BCAF attains 62.3% mIoU for material segmentation and 66.2% mIoU for plastic-type segmentation.

The main contributions are:

- A bidirectional, multi-scale fusion mechanism that aligns fine-grid RGB with coarse multi-slice HSI via localized cross-attention at native resolutions.
- An HSI-adapted Swin backbone with grouped spectral tokenization and factorized spatial-spectral attention, preserving spectral structure without early collapse.
- A simple two-phase training protocol (unimodal followed by multimodal fine-tuning) that stabilizes fusion and reuses unimodal checkpoints.
- A systematic study of RGB input resolution and HSI slice count ( $K=1-10$ ), revealing resolution-as-information gains and task-dependent optimal  $K$ .

The article is organized as follows: Section 2 reviews unimodal RGB/HSI segmentation and multimodal fusion. Section 3 presents BCAF and its constituent modules, including the adapted HSI Swin Transformer. Section 4 details the datasets (SpectralWaste, K3I-Cycling), training and evaluation protocols. Section 5 reports unimodal and fusion results, efficiency, and ablation studies. Section 6 concludes, while the Appendix provides additional visualizations and details.

## 2. Related Work

We review RGB feature extraction backbones, hyperspectral adaptations of these backbones, semantic segmentation architectures for RGB and HSI, and multimodal fusion strategies, and we identify the gap our method addresses.

### 2.1. Feature Extraction Backbones (RGB)

Early deep backbones for vision were convolutional neural networks (CNNs), which remain competitive for dense prediction under real-time constraints. Lightweight CNNs such as ENet [12] and ICNet [13]

are widely used as efficient feature extractors in industrial settings.

More recent work has adopted hierarchical Vision Transformer backbones tailored for dense prediction. Mixed Transformer (MiT, used in SegFormer) [14] and Swin Transformer [8] produce four-stage feature pyramids that are well suited to multi-scale decoding. MiT employs spatial-reduction attention to reduce complexity and underpins SegFormer-B0, which has been shown to enable real-time processing on waste-sorting data [10]. Swin uses shifted-window attention with complexity  $O(n \cdot M^2)$ , which scales linearly with the number of tokens for a fixed window size  $M$ . Off-the-shelf ImageNet pretraining and strong downstream performance have made Swin and MiT practical backbones for industrial deployments, including waste sorting [15, 6].

In this work, we adopt a Swin encoder as our RGB feature extractor.

## 2.2. HSI Adaptations of Feature Extraction Backbones

Hyperspectral imaging (HSI) provides strong spectral discrimination thanks to material-specific signatures, but its high channel count and often lower spatial resolution pose architectural and efficiency challenges. CNN-based HSI models include 1D spectral CNNs, 3D CNNs, and factorized 2D plus 1D designs. 3D CNNs capture joint spatial-spectral context but are computationally heavy, motivating factorized or dimensionality-reduced approaches under real-time constraints [16].

Transformer-based HSI backbones adapt image Transformers to handle spectral structure. SpectralFormer [17] builds on the ViT design [18], using patch embeddings and a Transformer encoder while applying self-attention along the spectral dimension to model band-wise dependencies. Subsequent variants incorporate spatial attention [19] or factorized spatial-spectral attention [20, 21] to jointly capture spatial and spectral context. However, many of these models are designed for patch-wise classification or small tiles rather than dense, real-time segmentation.

In our work, we adapt the hierarchical Swin backbone to HSI by grouping spectral bands into slices and applying factorized spatial-spectral attention, preserving spectral structure without early collapse while remaining compatible with multi-scale decoding.

## 2.3. Semantic Segmentation for RGB and HSI

Semantic segmentation networks map backbone features to pixel-wise predictions. Fully Convolutional Network (FCN) architectures [22] and U-Net [9] popularized encoder-decoder designs with skip connections

that recover spatial detail while aggregating semantic context. U-Net-like decoders remain standard due to their simplicity, efficiency, and strong performance across modalities.

For RGB imagery, subsequent architectures such as DeepLab [23] variants and Transformer-based decoders further improved segmentation quality, while lightweight designs like ENet [12], ICNet [13], and SegFormer-B0 [14, 10] target real-time inference. In industrial waste sorting, encoder-decoder models with hierarchical Transformer backbones (MiT, Swin) and U-Net-like decoders have been evaluated for multimaterial segmentation under throughput constraints [10, 6, 15]. These works demonstrate that real-time semantic segmentation on conveyor belts is feasible, but they also highlight the limitations of RGB-only cues for distinguishing visually similar materials, such as different plastic types [24].

For HSI, many models are formulated as patch classification or small-tile segmentation, and often focus on remote-sensing benchmarks [17, 19, 20, 21, 16]. When applied to dense segmentation, HSI is frequently processed with standard 2D backbones after early spectral collapse into a few bands or pseudo-RGB channels [10, 6, 24, 15], which limits the exploitation of fine-grained spectral information.

In this work, we follow the encoder-decoder paradigm and employ a shared U-Net-like decoder on top of Swin encoders for unimodal RGB, HSI, and their fusion.

## 2.4. Multimodal Fusion for Semantic Segmentation

Fusion strategies are commonly grouped into early, mid-level, and late fusion. Early fusion stacks channels across modalities, often requiring dimensionality reduction (e.g., principal component analysis, PCA), which can discard spectral structure. Mid-level fusion combines intermediate features via concatenation, summation, gating, or cross-attention, enabling richer cross-modal interactions at the cost of alignment complexity and compute. Late fusion merges decisions (e.g., logits), which is efficient but limits feature sharing.

Recent segmentation systems use feature-level cross/co-attention and multi-scale fusion to align heterogeneous cues. RGB-X methods such as CMX [4] and CANet [5] rely on up/downsampling to obtain matched spatial grids before fusion, and use cross-attention to exchange information between modalities. In industrial contexts, multimodal setups (e.g., RGB+NIR, RGB+depth) have shown that fusion can outperform unimodal baselines [7, 6].

For the modality combination of RGB and HSI, much of the fusion literature targets remote sensing, with fewer works addressing material discrimination and recycling. Ji et al. [24] apply an unaltered Swin Transformer backbone to plastic-flake recognition, using learned spectral channel selection and 2D convolutions in the embedding layer to collapse 224 bands and process data purely in the spatial domain. FusionSort [25] achieves strong performance on RGB-HSI/multispectral fusion by applying PCA to reduce the spectral dimension prior to fusion, again operating primarily in the spatial domain. Li et al. [6] propose the Hybrid Long-Range Feature Fusion Network (HLRFF-Net) and benchmark a broad set of state-of-the-art architectures for multimodal waste segmentation, but also rely on PCA-based band reduction (to three components) and resampling operations that reduce the effective RGB resolution during fusion.

### 2.5. Summary and Gap

In summary, RGB-based segmentation methods are efficient but struggle to reliably distinguish materials with similar appearance, especially different polymer types with overlapping color and texture cues [24].

HSI provides strong spectral cues for material discrimination [2, 3, 17] but typically has lower spatial resolution and higher computational cost than RGB sensors [16]. Moreover, many HSI networks are tailored to patch-wise classification rather than dense, real-time segmentation [17, 19, 20, 21].

In multimodal settings, prior RGB-HSI fusion methods frequently rely on spectral dimensionality reduction (e.g., PCA) and operate mainly in the spatial domain, collapsing the hyperspectral cube into a few pseudo-RGB channels and limiting the exploitation of fine-grained spectral structure [25, 6]. Furthermore, several architectures resize RGB data to the lower HSI resolution before fusion [6], discarding high-frequency spatial information that is crucial for segmenting small or thin objects on conveyor belts.

This creates a gap for a multimodal architecture that (i) preserves spectral structure during fusion, (ii) aligns RGB and HSI features with different native resolutions at multiple scales via cross-attention, and (iii) remains efficient enough for real-time deployment on industrial conveyor-belt data.

## 3. Methods

We first present an overview of the proposed bidirectional spectral cross-attention fusion (BCAF) architec-

ture. In subsequent subsections, we detail the modality-specific RGB and HSI backbones, the multimodal fusion mechanism and the shared segmentation head.

### 3.1. Architecture Overview

Figure 1 shows the BCAF architecture for semantic segmentation of co-registered RGB-HSI scenes that may differ in spatial resolution. BCAF comprises an RGB backbone (blue), an HSI backbone (red), bidirectional spectral cross-attention (dark green), a gated modality-fusion module (light green), and a shared U-Net-like decoder/segmentation head (grey). Modality-specific backbones enable unimodal training and reuse, while the shared decoder ensures comparable capacity across RGB-only, HSI-only, and fused models.

BCAF is designed around three requirements: (i) preserve high-resolution RGB detail, (ii) preserve HSI spectral structure without early collapse to a few bands, and (iii) remain efficient enough for real-time deployment on conveyor belts. To this end, both backbones follow a multi-scale encoder-decoder paradigm, and fusion is performed locally at the feature level via bidirectional cross-attention at the native grids of each modality.

**Encoder.** Both backbones follow a four-stage hierarchical Swin Transformer design with patch partition and patch merging. The RGB backbone performs spatial self-attention in shifted windows and acts as a pure spatial feature extractor for inputs  $H_f \times W_f \times 3$ . The adapted HSI Swin Transformer preserves the hyperspectral axis for inputs  $H_c \times W_c \times S$  by grouping spectral bands into  $K$  slices and applying a factorized spatial-spectral attention design to model spectral structure without early dimensionality reduction (e.g., PCA). The spatial ratio  $r$  satisfies  $H_f = rH_c$  and  $W_f = rW_c$  and remains constant across stages because both encoders downsample equally.

**Fusion and decoder.** Bidirectional local cross-attention aligns fine-grid RGB features with coarse-grid HSI features at native resolutions, followed by gated modality fusion. Unless otherwise stated, these modules are applied at all four stages. A single shared 2D decoder consumes the fused features via standard skip connections across stages, providing a lightweight architecture that reuses existing encoder-decoder designs.

**Notation.** We use channels-last tensor shapes. RGB features are  $H_f \times W_f \times C$  (fine grid), and HSI features are  $H_c \times W_c \times K \times C$  (coarse grid with  $K$  spectral slices).  $S$  denotes the number of raw HSI bands.  $K$  denotes the slice count after grouping.  $r$  denotes the integer spatial ratio with  $H_f = rH_c$ ,  $W_f = rW_c$ .  $C$  denotes the per-stage embedding width.  $D$  denotes the decoder width and  $N$

Table 1: Notation summary used throughout the methods.

Symbol	Meaning
$H_f, W_f$	Fine-grid (RGB) spatial size (height, width)
$H_c, W_c$	Coarse-grid (HSI) spatial size (height, width)
$r$	Spatial ratio: $H_f = r H_c, W_f = r W_c$
$K$	Number of HSI spectral slices retained after grouping
$S$	Number of raw HSI bands
$C$	Channel width per encoder stage
$D$	Decoder widths per upsampling stage
$N$	Number of foreground classes

denotes the number of classes. Implementation details and hyperparameters are provided in Section 4.2.

### 3.2. RGB Backbone

We adopt a hierarchical Swin Transformer encoder [8] as the RGB backbone. Its four-stage design with shifted-window self-attention offers a favorable trade-off between latency and accuracy for dense prediction tasks. The encoder outputs feature maps at  $\{1/4, 1/8, 1/16, 1/32\}$  of the input resolution, which are consumed by the shared decoder.

### 3.3. HSI Backbone

We adapt Swin Transformer to hyperspectral inputs with a factorized 2D+1D attention design that preserves spectral structure and supports unimodal HSI segmentation across variable spectral slice counts.

**Grouped patch partition.** Let  $S$  be the number of raw HSI bands. We replace the RGB patch partition over  $(4 \times 4 \times 3)$  with a grouped partition over  $(4 \times 4 \times R_G)$  bands. Each  $(4 \times 4 \times R_G)$  cube is projected by a convolution into one token, yielding a 3D token lattice of size  $(H_c/4) \times (W_c/4) \times K$  with  $C$  channels, with  $K = \lceil S/R_G \rceil$  spectral slices with exact padding, if needed (see Section 4.2). We refer to this backbone configuration as HSI- $K$ .

**Factorized attention ( $K > 1$ ).** At each stage, we apply standard Swin spatial window attention (and its shifted variant) independently to every spectral slice, followed by spectral multi-head self-attention along the slice axis ( $K$ ) at each spatial location. A learnable absolute spectral positional embedding provides ordering information for the  $K$  slices. The number of attention heads follows Swin Transformer defaults. This factorization preserves spectral structure while decoupling spatial and spectral modeling. A block-level view of the spectral attention appears in Figure 2 (left, red).

**Spatial-only patch merging.** Patch merging aggregates tokens only across spatial dimensions, halving spatial resolution at each stage while keeping the slice

count  $K$  unchanged. Consequently, spectral resolution remains consistent across all four stages.

**Outcome.** For  $K > 1$ , the adapted Swin Transformer backbone processes HSI cubes without early dimensionality reduction (e.g., PCA) and produces hierarchical 3D feature maps (height  $\times$  width  $\times K$  slices) at four spatial resolutions for subsequent semantic segmentation.

**HSI-1 (spectral collapse, 2D backbone).** When  $K=1$ , there is a single spectral slice and the pathway is purely 2D. We embed the  $S$ -band input with a learned  $4 \times 4 \times S \rightarrow C$  convolution and process it with a standard 2D Swin Transformer backbone and the shared 2D decoder. No spectral self-attention is applied. This baseline collapses the spectral axis at input and serves as a strong 2D reference for comparisons to  $K > 1$  settings that preserve spectral structure.

### 3.4. Spectral SE Pooling Module

We introduce a spectral squeeze-excitation (SE) pooling module that adaptively compresses the spectral axis (slice count  $K$ ), enabling a shared decoder across modalities. The design is inspired by SENet [26] and operates along the spectral dimension. Its block-level architecture is shown in Figure 2 (Middle/right, orange).

**Formulation.** Given HSI input features  $\mathbf{F}_{\text{hsi}} \in \mathbb{R}^{H \times W \times K \times C}$ , we first perform spatial global average pooling:

$$\mathbf{z} = \text{AvgPool}_{H,W}(\mathbf{F}_{\text{hsi}}) \in \mathbb{R}^{K \times C}.$$

Then we compute per-slice, per-channel gates with a two-layer bottleneck (applied independently for each  $k$ ):

$$\mathbf{a} = \sigma(f_2(\text{ReLU}(f_1(\mathbf{z})))) \in \mathbb{R}^{K \times C},$$

where  $f_1 : \mathbb{R}^C \rightarrow \mathbb{R}^{C_h}$  and  $f_2 : \mathbb{R}^{C_h} \rightarrow \mathbb{R}^C$  are pointwise ( $1 \times 1$ ) projections shared across  $k$ , with  $C_h = \max(\lfloor C/8 \rfloor, 8)$ . Finally, we aggregate across the spectral dimension:

$$\hat{\mathbf{F}}_{\text{hsi}} = \sum_{k=1}^K \mathbf{a}_k \odot \mathbf{F}_{\text{hsi},k} \in \mathbb{R}^{H \times W \times C},$$

where  $\mathbf{a}_k \in \mathbb{R}^{1 \times 1 \times C}$  is the gate for slice  $k$ ,  $\mathbf{F}_{\text{hsi},k} \in \mathbb{R}^{H \times W \times C}$  is the  $k$ -th spectral slice, and  $\odot$  denotes channel-wise multiplication broadcast over  $H \times W$ . This spectral-to-spatial reduction produces a 3D feature map suitable for 2D decoders.

### 3.5. Bidirectional Cross-Attention

We fuse RGB and HSI features using bidirectional, local cross-attention without pre-upsampling (cf. Figure 2, dark green). Let RGB features lie on a fine grid

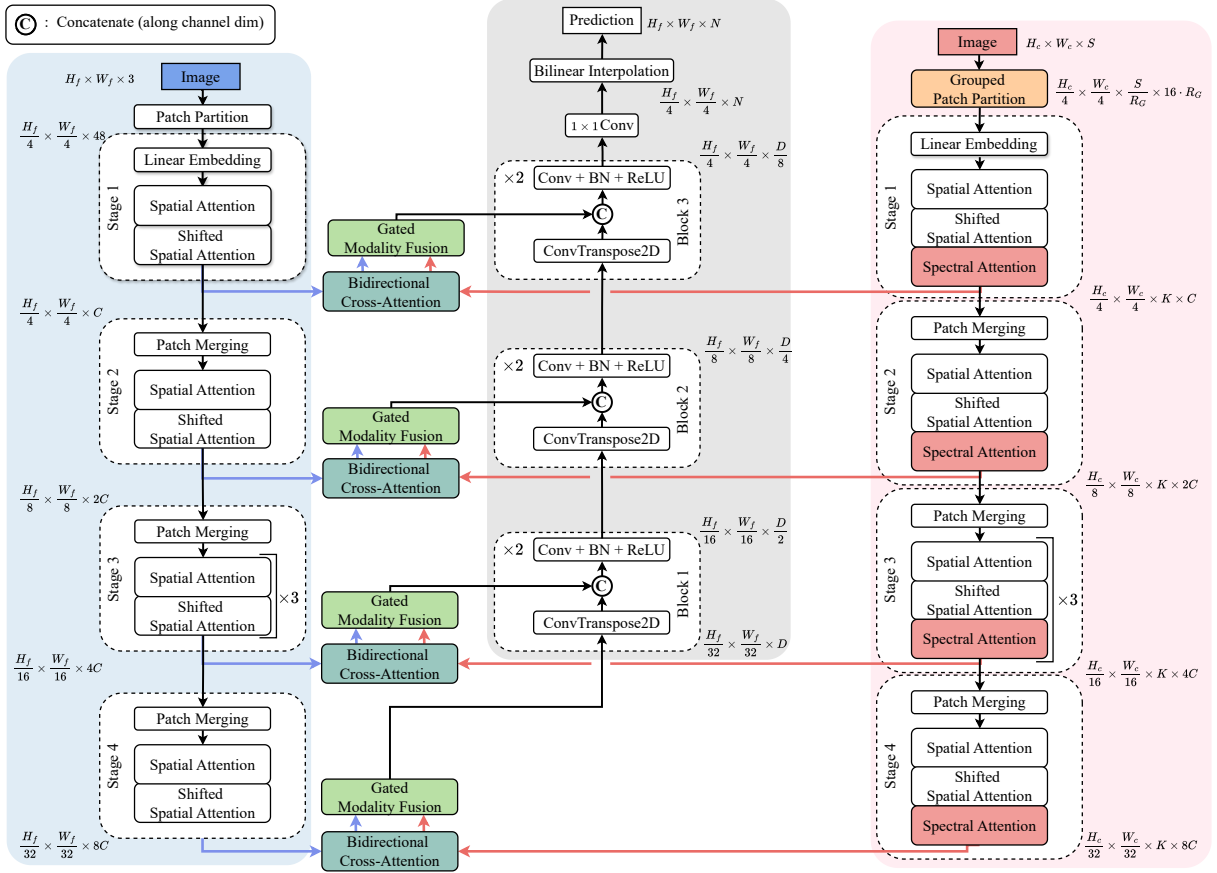


Figure 1: BCAF architecture. Left: RGB backbone (blue). Middle: shared decoder/segmentation head (grey). Right: HSI backbone (red) with bidirectional spectral cross-attention and gated modality fusion modules (green).

$H_f \times W_f$  and HSI features on a coarse grid  $H_c \times W_c$ , with  $H_f = rH_c$  and  $W_f = rW_c$  for integer  $r \geq 1$ . Each coarse HSI location  $(u, v)$  has  $K$  spectral slices and  $r^2$  co-registered RGB “children”. Attention is computed strictly within each coarse location  $(u, v)$  (no mixing across parents). Multi-head projections are used in both directions, where the per-head dimension is  $d_h = C/h$ . Per-head indices are omitted for clarity. At each stage we have the two sets of features:

$$\mathbf{F}_{\text{rgb}} \in \mathbb{R}^{H_f \times W_f \times C}, \quad \mathbf{F}_{\text{hsi}} \in \mathbb{R}^{H_c \times W_c \times K \times C}.$$

**Fine→Coarse (RGB queries HSI).** For each HSI parent  $(u, v)$ , we extract  $r^2$  RGB children  $X_{\text{rgb}}(u, v) \in \mathbb{R}^{r^2 \times C}$  via pixel-unshuffle [27] (space-to-depth), which rearranges every  $r \times r$  fine-grid neighborhood into a length- $r^2$  vector per  $(u, v)$ . The  $K$  HSI slices are  $X_{\text{hsi}}(u, v) \in \mathbb{R}^{K \times C}$ . With linear projections for queries, keys, and values,

$$Q_{\text{rgb}} = X_{\text{rgb}} W_Q^{r \rightarrow h}, \quad K_{\text{hsi}} = X_{\text{hsi}} W_K^{r \rightarrow h}, \quad V_{\text{hsi}} = X_{\text{hsi}} W_V^{r \rightarrow h},$$

the local scaled dot-product cross-attention at  $(u, v)$  is

$$O^{f \rightarrow c} = \text{softmax} \left( \frac{Q_{\text{rgb}} K_{\text{hsi}}^\top}{\sqrt{d_h}} \right) V_{\text{hsi}} \in \mathbb{R}^{r^2 \times C},$$

with softmax over the  $K$  keys. Outputs  $O^{f \rightarrow c}$  are re-assembled to the fine grid by pixel-shuffle (depth-to-space), linearly projected, fused with the RGB features via a residual connection, and passed through a position-wise FFN, preserving  $\mathbb{R}^{H_f \times W_f \times C}$ .

**Coarse→Fine (HSI queries RGB).** Symmetrically, at each parent  $(u, v)$  the  $K$  HSI slices attend to the  $r^2$  RGB children:

$$Q_{\text{hsi}} = X_{\text{hsi}} W_Q^{h \rightarrow r}, \quad K_{\text{rgb}} = X_{\text{rgb}} W_K^{h \rightarrow r}, \quad V_{\text{rgb}} = X_{\text{rgb}} W_V^{h \rightarrow r},$$

$$O^{c \rightarrow f} = \text{softmax} \left( \frac{Q_{\text{hsi}} K_{\text{rgb}}^\top}{\sqrt{d_h}} \right) V_{\text{rgb}} \in \mathbb{R}^{K \times C},$$

with softmax over the  $r^2$  keys. These updates are added residually to the HSI slices and passed through a position-wise FFN, preserving  $\mathbb{R}^{H_c \times W_c \times K \times C}$ .

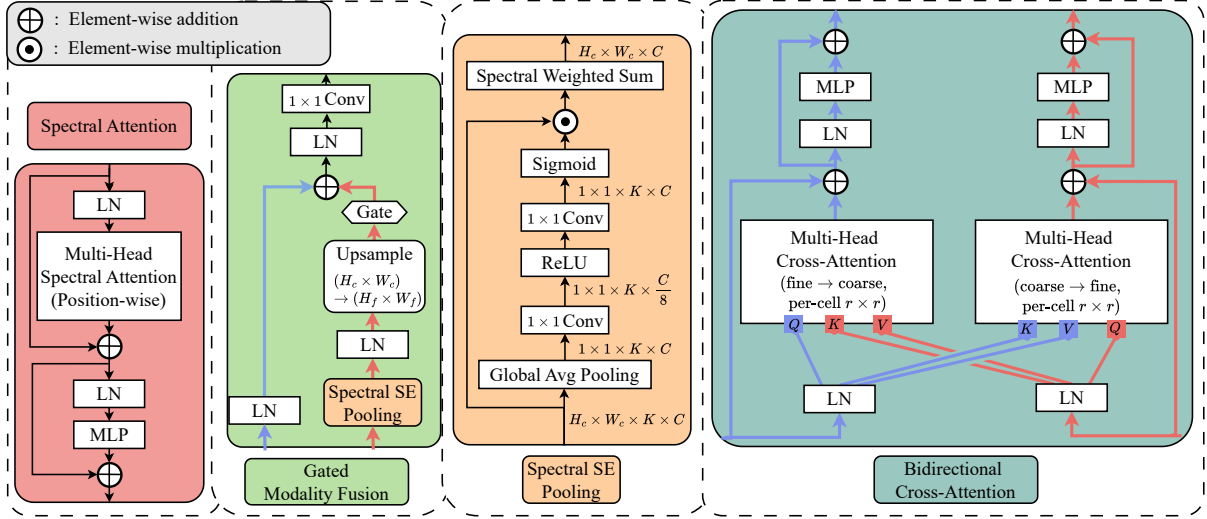


Figure 2: Module details. Left (red): position-wise spectral self-attention. Middle/left (light-green): gated modality fusion. Middle/right (orange): spectral SE Pooling module. Right (dark-green): bidirectional cross-attention modules.

**Special case  $r=1$ .** When grids coincide, RGB→HSI reduces to  $1 \times K$  attention and HSI→RGB reduces to single-key attention at each location.

### 3.6. Modality Fusion Module

The modality-fusion module merges the RGB and HSI branches into a single 2D feature map per stage for the shared decoder. It first applies spectral SE pooling (Section 3.4) to compress the HSI slice axis while preserving the channel dimension, then upsamples the result by  $r$  (nearest-neighbor) to match the RGB grid, yielding  $\hat{\mathbf{F}}_{\text{hsi}}$  (identity when  $r=1$ ). Both branches are LayerNorm (LN) normalized. A learned per-channel gate  $\alpha \in \mathbb{R}^C$  (sigmoid-activated) modulates the HSI contribution, and the fused output is

$$\mathbf{F}_{\text{fuse}} = \text{LN} \left( \text{LN}(F_{\text{rgb}}) + \sigma(\alpha) \odot \text{LN}(\hat{\mathbf{F}}_{\text{hsi}}) \right) \in \mathbb{R}^{H_f \times W_f \times C},$$

where  $\sigma(\cdot)$  denotes the sigmoid and  $\odot$  denotes channel-wise multiplication broadcast over  $H_f \times W_f$ . The module is applied at all four stages after cross-attention, introduces minimal overhead ( $O(H_f W_f C)$ ), preserves spatial resolution, and allows adaptive control of HSI influence relative to RGB.

### 3.7. Segmentation Decoder

We use a single, 2D U-Net-like decoder across all settings (RGB-only, HSI-only, and RGB-HSI fusion). The decoder expects 2D feature maps at four hierarchical stages and is identical in all cases. Features from the backbones are first channel-aligned via  $1 \times 1$

adapters to a common width  $D$  per stage. Starting from the deepest stage, the decoder performs three upsampling steps (transpose-convolution with stride 2), each followed by Conv-BatchNorm-ReLU refinement. Lateral skip connections from shallower stages are concatenated at matching resolutions to preserve fine detail.

A final  $1 \times 1$  classifier maps to  $N$  classes. Logits are resized to input resolution by bilinear interpolation if needed. In the HSI-only path, each stage is passed through spectral SE pooling to collapse the slice axis ( $K$ ) into a 2D map prior to channel alignment. In fusion, the fused 2D features are channel-aligned and decoded identically.

**Losses.** We optimize a weighted sum of cross-entropy and Dice losses:

$$\mathcal{L} = 0.5 \mathcal{L}_{\text{CE}} + 1.5 \mathcal{L}_{\text{Dice}}.$$

Let  $z \in \mathbb{R}^{H \times W \times (N+1)}$  be the logits over  $N$  foreground classes plus background. Let  $p = \text{softmax}(z)$  denote class probabilities, and  $Y \in \{0, 1\}^{H \times W \times (N+1)}$  the one-hot labels.

$$\mathcal{L}_{\text{CE}} = -\frac{1}{HW} \sum_{h=1}^H \sum_{w=1}^W \sum_{n=1}^{N+1} w_n Y_{n,h,w} \log p_{n,h,w},$$

with median-frequency class weights computed on the training set (background included) to compensate for pixel-level class imbalance:

$$w_n = \frac{\text{median}\{f_k \mid f_k > 0\}}{f_n + \varepsilon_w}, \quad \varepsilon_w = 10^{-6}.$$

Dice loss is computed on probabilities with  $\epsilon = 1.0$ , averaged uniformly over all  $N+1$  classes (background included):

$$\text{Dice}_n = \frac{2 \sum_{h,w} p_{n,h,w} Y_{n,h,w} + \epsilon}{\sum_{h,w} p_{n,h,w} + \sum_{h,w} Y_{n,h,w} + \epsilon},$$

$$\mathcal{L}_{\text{Dice}} = 1 - \frac{1}{N+1} \sum_{n=1}^{N+1} \text{Dice}_n.$$

## 4. Experimental Setup

We evaluate our approach on two multimodal RGB-HSI datasets: the public SpectralWaste dataset[10] and our novel K3I-Cycling dataset. K3I-Cycling is evaluated under two label taxonomies: K3I-Material (primary materials) and K3I-Plastic (plastic-type distinctions). We first describe the datasets, splits, and preprocessing, then detail training and implementation, baselines, and evaluation protocols.

### 4.1. Datasets

**SpectralWaste.** This multimodal benchmark was collected in an operational plastic-waste sorting facility, reflecting realistic indoor recycling lines with densely packed, partially occluded, and contaminated items [10]. Each scene includes a conventional RGB image (Teledyne DALSA Linea, initial resolution  $1200 \times 1184$ ) and a near-infrared hyperspectral cube (Specim FX17, initial  $600 \times 640 \times 224$ ), pairing color cues with material-sensitive spectral signatures. The released subset provides 852 non-overlapping images with 2,059 instance annotations across six categories: basket, film, filament, video tape, cardboard, and trash bag. We use the official split of 514/167/171 for train/validation/test. The public release offers aligned RGB at  $256 \times 256$  and HSI at  $256 \times 256 \times 224$ .

For our resolution analysis, we keep HSI fixed at  $256 \times 256$  and vary only the RGB input resolution. Specifically, we start from the provided  $256 \times 256$  RGB images and upsample them to  $512 \times 512$ ,  $1024 \times 1024$ , and  $2048 \times 2048$ , yielding a *more pixels, same information* regime where the effective spatial information is unchanged but the number of pixels processed by the network increases.

**K3I-Cycling.** K3I-Cycling is a lightweight packaging dataset captured with a RGB (SW-4000T-10GE from JAI) and a hyperspectral line-scan camera (FX17e from SPECIM). Samples were transported on a conveyor at 0.2 m/s with mixed materials and realistic residue/contamination. Items were post-consumer lightweight packaging provided by Lobbe RSW GmbH.

Example scenes are shown in Figure 3. The dataset contains 354 co-registered RGB-HSI pairs with 4,855 labelled object instances. RGB images have  $4096 \times 4096$  resolution, HSI cubes have  $512 \times 512 \times 205$  with 205 being the number of spectral channels linearly distributed from 964 nm to 1668 nm. We adopt a 214/70/70 train/val/test split. All foreground objects are assigned a semantic label. Background corresponds to the conveyor and non-object pixels. We plan to publicly release the RGB images in the future (first subset released), with an expanded set of images and sensors.

RGB and HSI images are co-registered via marker-based calibration. Circular fiducials at the start and end of each of 10 runs are automatically detected. We first rectify the RGB images and correct the nonlinear pixel distribution along the recording line to establish an orthogonal, linearly spaced base coordinate system. A polynomial mapping between RGB and HSI feature coordinates is then fitted, and HSI images are warped into the RGB coordinate system using `cv2.remap` (OpenCV-Python).

We evaluate two taxonomies and refer to them as:

- **K3I-Material** (4 primary materials): plastic (2,937 instances), paper/cardboard (1,072), metal (266), other (580).
- **K3I-Plastic** (8 plastic-related classes): no plastic (1,033), LDPE (low-density polyethylene, 813), PP (polypropylene, 765), PET (polyethylene terephthalate, 349), EPS (expanded polystyrene, 184), HDPE (high-density polyethylene, 157), PS (polystyrene, 111), other plastic (1,443).

Counts refer to instance-level annotations across the full dataset. Mean normalized spectra for all classes are shown in the Appendix (see Figure 8). We treat 'other' (Material) and 'other plastic' (Plastic) as valid foreground classes and include them in training and evaluation (they count toward  $N$ ). In both taxonomies, 'background' denotes the conveyor belt and non-object pixels. For K3I-Plastic, 'no plastic' is a foreground class for non-plastic objects (e.g., paper/cardboard, metal) and is distinct from background. The 'other plastic' class is used for plastics which are none of the predefined classes or when a plastic item cannot be reliably assigned to one of the listed polymer types (e.g., heavy contamination or uncertain spectra).

**Input resolutions for K3I-Cycling.** K3I-Material/Plastic has native RGB resolution  $4096 \times 4096$  and HSI resolution  $512 \times 512$ . We downsample HSI to  $256 \times 256$  for all experiments.

For RGB, we consider two regimes:

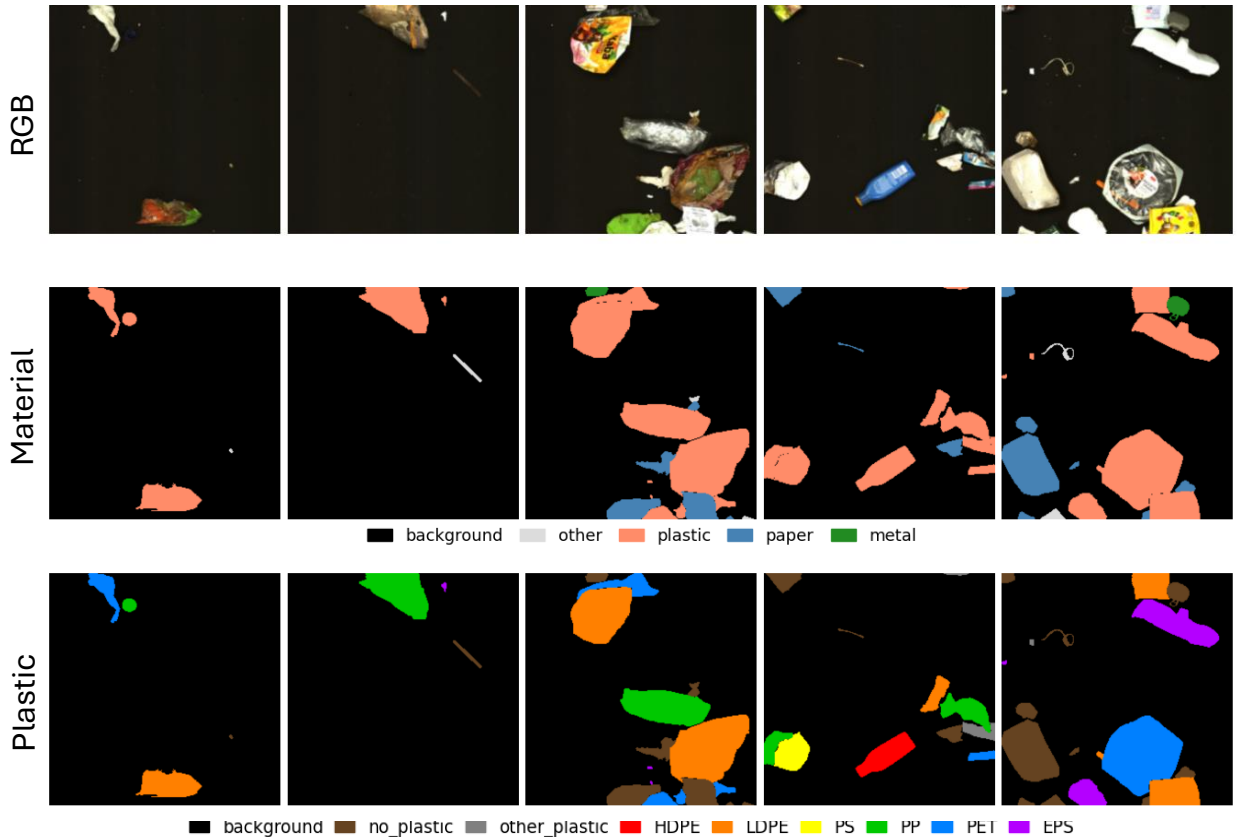


Figure 3: Samples from the K3I-Cycling dataset. Rows (top to bottom): RGB image, labelled K3I-Material masks, labelled K3I-Plastic masks.

- (i) **Small-resolution regime** (*more pixels, same information*): we first downsample the RGB image to  $256 \times 256$ , then upsample this low-resolution image to  $256 \times 256$ ,  $512 \times 512$ ,  $1024 \times 1024$ , and  $2048 \times 2048$ . This mirrors the SpectralWaste setting, increasing pixel count without adding spatial information.
- (ii) **Native-resolution regime** (*more pixels, more information*): we downsample directly from the native  $4096 \times 4096$  to  $2048 \times 2048$ ,  $1024 \times 1024$ , and  $512 \times 512$ , allowing us to quantify the impact of retaining higher spatial information on segmentation performance.

#### 4.2. Training and Implementation Details

**Training regime.** Training proceeds in two phases with identical optimization hyperparameters: (i) unimodal training of RGB and HSI models (trained independently), and (ii) multimodal fusion fine-tuning that initializes from the unimodal checkpoints and adds bidirectional cross-attention. Each phase runs for 1000

epochs on SpectralWaste and 300 epochs on K3I-Material/Plastic, yielding a comparable number of optimization steps given the smaller size of K3I-Cycling. During fusion, all parameters (both backbones, cross-attention, fusion gates, and decoder) are unfrozen unless noted otherwise.

**RGB backbone configuration.** We adopt Swin Transformer Tiny (Swin-T) [8] as the RGB encoder with patch size 4, window size 7, shift 3, attention depths (2, 2, 6, 2), and heads (3, 6, 12, 24). Embedding dimensions expand across stages (96, 192, 384, 768). DropPath is linearly scheduled to 0.3. We initialize from `swin_tiny_patch4_window7_224` [28].

**HSI backbone configuration.** For the HSI backbone we adapt Swin-T as described in Section 3.3. We initialize from `swin_tiny_patch4_window7_224` [28] where shapes match and randomly initialize spectral-specific layers. For example, for adapted Swin-T attention depths of (3, 3, 9, 3), the first (2, 2, 6, 2) blocks per stage are initialized from the pretrained Swin-T weights, while the additional blocks (1, 1, 3, 1) are initialized randomly.

To create the 3D tokenization, we group contiguous bands into  $K$  slices. When the raw band count  $S \in \{224, 205\}$  is not divisible by  $K$ , we zero-pad to the nearest multiple and set the group size  $R_G = S_{\text{pad}}/K$ . We adopt a shared-kernel embedding: a single  $4 \times 4 \times R_G \rightarrow C$  convolution is applied to each spectral group with weights shared across groups, producing  $(H/4) \times (W/4) \times K$  tokens. For SpectralWaste (224 bands), this yields  $R_G = \{224, 75, 45, 32, 23\}$  for  $K = \{1, 3, 5, 7, 10\}$ , obtained by padding to  $S_{\text{pad}} = 225$  for  $K \in \{3, 5\}$  and to 230 for  $K = 10$ . For K3I-Material/Plastic (205 bands), this yields  $R_G = \{205, 69, 41, 30, 21\}$  for  $K = \{1, 3, 5, 7, 10\}$ , obtained by padding to  $S_{\text{pad}} = 207$  for  $K = 3$  and to 210 for  $K \in \{7, 10\}$ .

**BCAF fusion configuration.** We use one cross-attention block per stage to limit computational overhead. The number of heads follows the backbones: (3, 6, 12, 24) across the four stages. Cross-attention and fusion parameters are randomly initialized.

**Shared decoder configuration.** For the three decoder blocks with channel widths  $D = [256, 128, 64]$  we use dropout 0.0 for RGB-only models and 0.1 for HSI-only and fusion models.

**Data augmentation (train only).** We apply identical spatial augmentations to RGB and HSI: random rotation ( $[-5^\circ, +5^\circ]$ ), scale ( $[0.8, 1.3]$ ), random crop to the target input resolution, and horizontal/vertical flips (each with probability 0.5). RGB photometric jitter is applied with probability 0.8 (brightness/contrast/saturation 0.2, hue 0.03). HSI spectral jitter uses additive  $\mathcal{U}[-0.10, 0.10]$  and multiplicative  $\mathcal{U}[0.90, 1.10]$ , applied only to non-zero elements.

**Background masking for HSI.** To prevent interpolation bleed of non-zero foreground into the zero-valued HSI background, we construct a binary foreground mask directly from the HSI (non-zero spectrum = 1, background = 0), apply the same geometric transforms to the mask using nearest-neighbor, and multiply the transformed mask with the transformed HSI to re-zero the background. This preserves a strictly zero background, avoids bias in downstream normalization, and does not rely on any label information.

**Normalization.** RGB uses ImageNet statistics ( $\mu_{\text{RGB}} = [0.485, 0.456, 0.406]$ ,  $\sigma_{\text{RGB}} = [0.229, 0.224, 0.225]$ ). HSI uses masked per-channel standardization computed over the training split, excluding background (zeros). For the train split, normalization is applied at the end of data augmentation pipeline.

**Optimization and schedule.** We use AdamW (weight decay 0.01) with target learning rates by pa-

rameter group: head  $1 \times 10^{-4}$ , backbone (pretrained)  $1 \times 10^{-5}$ , backbone (random init)  $1 \times 10^{-4}$ . The schedule uses a 5-epoch linear warm-up to the target learning rate (LR), then polynomial decay (power 0.9) to the end of training. The effective batch size is 8 via 4-step gradient accumulation (micro-batch 2 per step). We follow `timm` defaults and do not apply weight decay to normalization and bias parameters.

**Seeds and reproducibility.** We train with five seeds (40-44) on SpectralWaste and three seeds (40-42) on K3I-Cycling, applied to PyTorch, NumPy, data loading, and CUDA. We report mean  $\pm$  std over the corresponding seeds. We enable automatic mixed precision (AMP) and do not use gradient clipping.

#### 4.3. Baselines

**RGB encoder baselines.** We compare against SegFormer’s MiT (Mix Transformer) encoders MiT-B0 and MiT-B2 [14]. To equalize decoder capacity across backbones, we replace SegFormer’s original MLP head with our shared U-Net-like decoder (Section 3.7). Initialization uses ImageNet pretrained MiT weights, and training follows exactly the same data preprocessing, augmentations, optimization, and schedules as for our Swin-T RGB backbone (Section 4.2).

**Logit fusion (late-fusion baseline).** As a simple modality-combination baseline, we fuse unimodal predictions via logit fusion. We load unimodal RGB and HSI checkpoints, obtain their per-pixel logits, bilinearly resize the HSI logits to the RGB grid (`align_corners=false`) if needed, concatenate the two along the channel dimension, and apply a learned  $1 \times 1$  convolution to produce fused logits. A softmax yields the final probabilities. Training follows exactly the same data preprocessing, augmentations, optimization, and schedules as for our BCAF Section 4.2. For logit fusion, the unimodal RGB/HSI backbones and the  $1 \times 1$  fusion layer are fine-tuned jointly.

#### 4.4. Metrics and Evaluation Protocol

We report per-class Intersection-over-Union (IoU) and mean IoU (mIoU). For each class  $c$ ,

$$\text{IoU}_n = \frac{TP_n}{TP_n + FP_n + FN_n}, \quad (1)$$

where  $TP_n$ ,  $FP_n$ , and  $FN_n$  denote the number of true-positive, false-positive, and false-negative pixels for class  $n$ , accumulated over the evaluation split. The mIoU is the unweighted mean over the evaluated classes  $N$ , excluding the background class:

$$\text{mIoU} = \frac{1}{|N|} \sum_{n \in N} \text{IoU}_n. \quad (2)$$

On SpectralWaste (ground-truth masks  $256 \times 256$ ), model outputs produced at  $512 \times 512$ ,  $1024 \times 1024$ , and  $2048 \times 2048$  are downsampled to  $256 \times 256$  by bilinear interpolation of the raw logits (`align_corners=false`), followed by `arg max` over classes, before computing IoU with the original labels to ensure comparability with prior work.

We also assess efficiency and complexity by reporting throughput (images/s) and GFLOPs. Measurements use synthetically generated inputs at the specified resolutions: RGB  $256 \times 256 \times 3$ ,  $512 \times 512 \times 3$ ,  $1024 \times 1024 \times 3$ ,  $2048 \times 2048 \times 3$  and HSI  $256 \times 256 \times S$  with  $S \in \{224, 225, 230\}$  depending on spectral padding. Throughput is measured on a single NVIDIA GeForce RTX 4090 with cuDNN autotuning enabled, `model.eval()`, `torch.no_grad()`, batch size = 1, and FP16 (AMP) disabled (FP32 inference). For each of 20 runs, we perform 100 warm-up forward passes to stabilize kernels, followed by 1000 timed passes using CUDA events with explicit GPU synchronization. We report the median over runs.

We measure GFLOPs with `fvcore` using matched dummy inputs for unimodal models. For fusion models, encoder GFLOPs are measured with `fvcore`, while cross-attention, decoder, and adapter layers are computed analytically from feature map dimensions, token dimensions as well as the the number of spectral groups  $S$ .

## 5. Results

This section presents the empirical evaluation of our unimodal RGB and HSI pipelines and our multimodal BCAF. We first analyze unimodal performance to isolate the effects of RGB spatial input resolution and the number of HSI spectral slices  $K$  (Sections 5.1 and 5.2). We then compare BCAF against a late-fusion baseline using learned logit fusion (Section 5.3). We further assess computational efficiency (Section 5.4), and conduct ablations (Section 5.5) on key HSI backbone components (grouped embedding and spectral attention) as well as on fusion-stage placement within BCAF.

As metrics we report class-wise Intersection-over-Union (IoU, %) and mean IoU (mIoU, %), alongside images per second (images/s), parameter counts (M), and GFLOPs. Higher is better for IoU/mIoU/images/s ( $\uparrow$ ), and lower is better for Params/GFLOPs ( $\downarrow$ ). SpectralWaste results are averaged over 5 seeds and K3I-Cycling results over 3 seeds (mean  $\pm$  std), under a consistent training protocol for fair comparison.

Qualitative results on SpectralWaste are shown in Figure 4, with detailed quantitative results in Table 2.

For K3I-Cycling, material segmentation and plastic-type segmentation are reported in Table 3 and Table 4, respectively. Additional qualitative examples for plastic-type are shown in Figure 5. Material-segmentation examples are provided in the appendix.

### 5.1. RGB: effect of input resolution

We analyze the RGB backbone under the two resolution protocols defined in Section 4.1: (i) scaling-only (inputs upsampled but evaluated at  $256 \times 256$ , no new scene detail), and (ii) information-preserving (downsampling the native  $4096 \times 4096$  acquisition to the target size, larger inputs retain more spatial detail). Trends are visualized in Figure 6 (left).

**Scaling-only (SpectralWaste and K3I-Material/Plastic).** Moderate upsampling ( $256 \rightarrow 512 \rightarrow 1024$ ) improves segmentation by several percentage points, then degrades when pushed too far (2048). Because evaluation remains at  $256 \times 256$ , these gains reflect better optimization and more effective receptive-field/window utilization rather than additional spatial information. Excessive upscaling eventually hurts generalization. See Tables 2 to 4.

**Information-preserving (K3I-Material/Plastic).** When working with native resolution images ( $4096 \times 4096$ ), increasing the input size  $256 \rightarrow 512 \rightarrow 1024 \rightarrow 2048$  yielding consistent gains. At the same nominal input sizes, the information-preserving protocol outperforms scaling-only, indicating that improvements are driven by genuinely retained scene detail (finer edges, small instances, textures) rather than scaling alone. We do not report 4096 inputs due to computational constraints. See Tables 3 and 4.

**Backbone comparison (MiT vs. Swin).** At an input resolution of 256 MiT-B2 outperforms Swin-T. When increasing the input size, swin’s shifted-window design benefits more from, whereas MiT’s spatial-reduction attention saturates earlier. See Table 2.

### 5.2. HSI: effect of spectral slices

We vary the number of spectral slices  $K$  by grouping contiguous bands in the HSI backbone (Section 4.2). We find that optimal  $K$  selection is driven by task difficulty. Increasing  $K$  exposes richer spectral structure, while decreasing  $K$  denoises/regularizes.

**Texture-dominated (SpectralWaste, K3I-Material).** Here we find that small to intermediate  $K$  is sufficient. Collapsing the spectrum ( $K=1$ , 2D Swin without spectral attention) remains competitive for unimodal HSI. Large  $K$  can even degrade segmentation

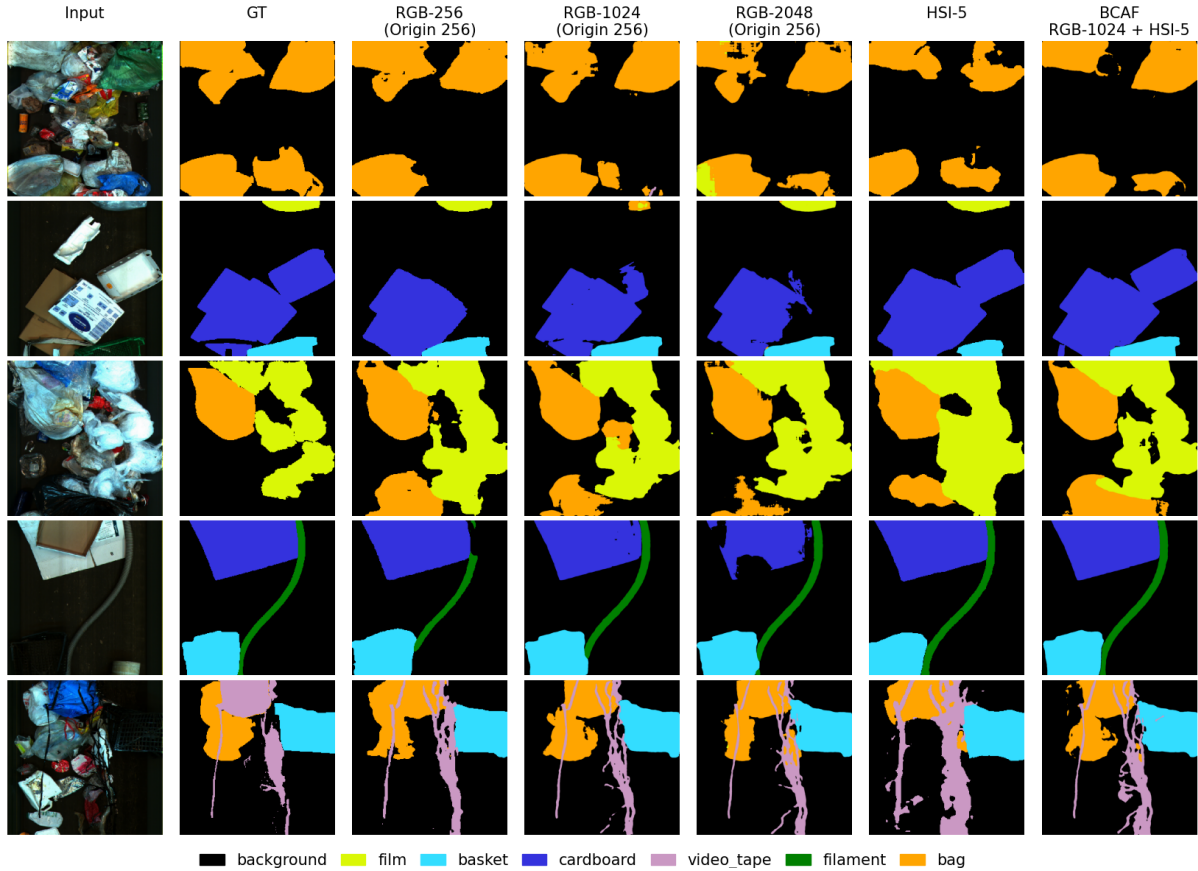


Figure 4: Qualitative results on SpectralWaste. Shown are Swin-T RGB at 256/1024/2048, adapted Swin-T HSI with  $K=5$  slices, and our best BCAF (RGB 1024 + HSI-5).

Table 2: SpectralWaste: quantitative comparison of SegFormer (MiT-B0/B2), Swin-T (RGB), adapted Swin-T (HSI- $K$ ), BCAF, and Logit fusion across RGB resolutions and HSI slice counts.

Backbone	Modality	IoU (%) $\uparrow$						mIoU (%) $\uparrow$	Img./s $\uparrow$	Params (M) $\downarrow$	GFLOPs $\downarrow$
		Film	Basket	Card.	Tape	Filam.	Bag				
MiT-B0	RGB-256	74.8	76.3	76.7	31.0	52.0	62.0	$62.1 \pm 1.6$	226.3	7.739	2.983
MiT-B0	RGB-1024	70.1	80.0	73.8	43.0	74.2	60.5	$66.9 \pm 1.1$	77.1	7.739	63.325
MiT-B2	RGB-256	76.9	81.1	72.2	39.8	67.8	67.5	$67.6 \pm 0.8$	134.4	41.866	13.817
MiT-B2	RGB-1024	76.4	81.1	64.4	46.7	78.5	66.6	$69.0 \pm 0.8$	30.6	41.866	279.458
Swin-T	RGB-256	76.1	77.9	76.1	38.1	59.2	67.4	$65.8 \pm 1.2$	141.0	32.176	9.862
Swin-T	RGB-512	78.2	81.4	79.2	45.0	71.4	71.6	$71.1 \pm 0.6$	134.6	32.176	35.571
Swin-T	RGB-1024	75.3	82.9	78.4	45.4	77.5	70.2	<b><math>71.6 \pm 0.3</math></b>	60.4	32.176	138.683
Swin-T	RGB-2048	69.1	82.7	69.2	46.6	76.4	66.2	$68.4 \pm 0.8$	15.0	32.176	546.316
Swin-T	HSI-1	67.4	71.5	84.9	26.8	56.9	57.7	<b><math>60.9 \pm 0.2</math></b>	141.0	32.176	9.906
Adapted Swin-T	HSI-3	68.3	66.9	86.8	24.5	55.7	56.1	$59.7 \pm 0.7$	114.1	45.459	34.158
Adapted Swin-T	HSI-5	68.2	67.6	86.4	23.8	56.4	59.6	$60.3 \pm 0.9$	118.8	45.417	54.343
Adapted Swin-T	HSI-7	66.3	64.7	83.5	24.2	58.1	57.1	$59.0 \pm 1.5$	90.8	45.402	74.547
Adapted Swin-T	HSI-10	67.2	64.4	85.5	21.0	54.5	54.3	$57.8 \pm 1.2$	67.9	45.394	104.902
Logit Fusion	RGB-1024 + HSI-5	76.5	82.2	83.9	47.2	74.9	70.9	$72.6 \pm 0.8$	38.8	77.593	209.797
BCAF	RGB-256 + HSI-5	78.3	80.1	88.2	40.0	70.3	69.7	$71.1 \pm 0.4$	54.4	101.296	78.284
BCAF	RGB-512 + HSI-5	80.3	84.7	90.1	47.2	76.9	73.2	$75.4 \pm 0.2$	54.9	101.296	119.007
BCAF	RGB-1024 + HSI-1	78.8	84.6	87.7	50.0	80.9	72.3	$75.7 \pm 0.5$	39.4	88.055	210.964
BCAF	RGB-1024 + HSI-5	78.1	85.0	90.8	50.0	80.4	73.8	<b><math>76.4 \pm 0.4</math></b>	31.4	101.296	282.176

Table 3: K3I-Material (segmentation): quantitative comparison of Swin-T (RGB), adapted Swin-T (HSI- $K$ ), and BCAF across RGB resolutions and HSI slice counts.

Backbone	Modality	RGB		other	IoU (%) $\uparrow$			mIoU (%) $\uparrow$
		Origin Res	Input Res		plastic	paper	metal	
Swin-T	RGB	256	256	15.7	76.5	44.7	7.1	36.0 $\pm$ 0.4
Swin-T	RGB	256	512	25.4	80.2	50.9	16.3	43.3 $\pm$ 0.4
Swin-T	RGB	256	1024	24.6	81.2	53.4	18.6	44.4 $\pm$ 0.4
Swin-T	RGB	256	2048	27.1	80.7	51.5	15.5	43.7 $\pm$ 0.6
Swin-T	RGB	4096	512	27.2	80.2	51.5	23.8	45.7 $\pm$ 0.5
Swin-T	RGB	4096	1024	33.8	85.3	61.5	33.4	53.5 $\pm$ 0.6
Swin-T	RGB	4096	2048	33.7	87.8	70.1	38.6	<b>57.6 <math>\pm</math> 0.4</b>
Adapted Swin-T	HSI-1			10.1	83.9	72.7	28.9	48.9 $\pm$ 0.6
Adapted Swin-T	HSI-3			18.2	82.5	73.3	26.3	<b>50.1 <math>\pm</math> 0.9</b>
Adapted Swin-T	HSI-5			21.4	82.4	73.4	19.8	49.2 $\pm$ 0.8
Adapted Swin-T	HSI-7			19.9	79.5	71.8	18.0	47.3 $\pm$ 1.3
Adapted Swin-T	HSI-10			16.1	79.5	70.2	15.8	45.4 $\pm$ 0.8
Logit Fusion	RGB+HSI-3	4096	1024	33.9	89.7	78.1	29.9	57.9 $\pm$ 1.8
BCAF	RGB+HSI-3	4096	1024	36.2	90.9	80.8	41.4	<b>62.3 <math>\pm</math> 1.1</b>

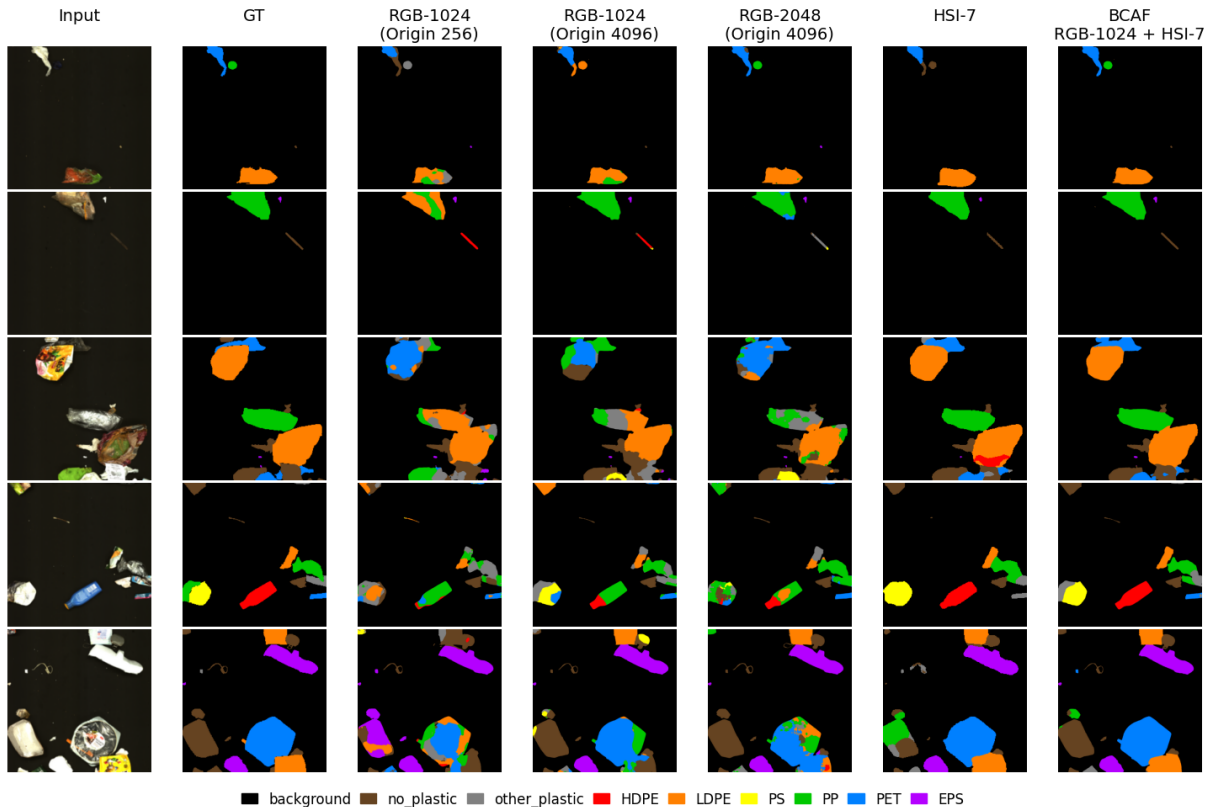


Figure 5: Qualitative results on K3I-Plastic (segmentation). Shown are Swin-T RGB at 1024 and 2048, adapted Swin-T HSI with  $K=7$  slices, and our best BCAF (RGB 1024 + HSI-7).

performance due to amplified noise and limited need for fine spectral detail. The unimodal HSI-RGB gap is modest in these settings, indicating that texture/shape cues already carry most of the discriminative signal.

See Tables 2 and 3.

**Visually similar (K3I-Plastic).** When material distinction is impossible using only visual cues, explicit spectral modeling is essential. Performance increases

Table 4: K3I-Plastic (segmentation): quantitative comparison of Swin-T (RGB), adapted Swin-T (HSI- $K$ ), and BCAF across RGB resolutions and HSI slice counts.

Backbone	Modality	RGB		no_plastic		other_plastic		IoU (%) $\uparrow$						mIoU (%) $\uparrow$
		Origin Res	Input Res	HDPE	LDPE	PS	PP	PET	EPS					
Swin-T	RGB	256	256	41.4	22.9	13.8	33.4	6.7	18.1	19.1	55.5	26.3 $\pm$ 0.6		
Swin-T	RGB	256	512	44.3	20.5	17.3	41.2	4.4	20.3	19.1	52.0	27.4 $\pm$ 1.1		
Swin-T	RGB	256	1024	51.5	24.5	16.3	40.6	9.0	25.8	22.3	62.6	31.6 $\pm$ 0.8		
Swin-T	RGB	256	2048	52.4	25.8	14.1	41.6	9.5	25.3	23.1	54.5	30.8 $\pm$ 0.5		
Swin-T	RGB	4096	512	49.7	25.6	18.5	41.6	13.2	24.2	23.3	68.5	33.1 $\pm$ 0.6		
Swin-T	RGB	4096	1024	56.3	26.4	19.8	46.3	9.7	32.6	30.8	82.2	38.0 $\pm$ 0.1		
Swin-T	RGB	4096	2048	63.2	27.6	15.0	47.1	11.5	32.0	28.6	90.5	<b>39.4 <math>\pm</math> 0.2</b>		
Adapted Swin-T	HSI-1			65.0	31.3	26.6	41.2	26.6	36.9	50.6	71.6	43.7 $\pm$ 1.1		
Adapted Swin-T	HSI-3			68.2	34.1	47.0	65.5	67.3	60.8	71.0	85.3	62.4 $\pm$ 2.3		
Adapted Swin-T	HSI-5			69.7	31.9	46.7	65.6	61.3	63.6	73.8	79.6	61.5 $\pm$ 1.7		
Adapted Swin-T	HSI-7			69.5	35.8	56.6	68.0	65.0	62.9	74.9	82.6	<b>64.4 <math>\pm</math> 1.7</b>		
Adapted Swin-T	HSI-10			68.4	36.9	54.0	66.3	65.8	63.6	74.3	85.1	64.3 $\pm$ 0.8		
Logit Fusion	RGB+HSI-7	4096	1024	69.7	31.6	45.6	65.6	46.8	63.5	55.3	85.8	58.0 $\pm$ 4.5		
BCAF	RGB+HSI-7	4096	1024	77.8	39.8	39.9	71.9	63.7	67.0	75.9	93.8	<b>66.2 <math>\pm</math> 1.7</b>		

steadily with  $K$  and peaks at moderate-to-large  $K$  (around 7, with 10 close). Here, unimodal HSI with multi-slice spectral attention yields substantial mIoU gains over both unimodal RGB and HSI-1 (2D-only), confirming that polymer separation is governed by spectral signatures rather than texture or color. This shows the value of our HSI-adapted Swin, in contrast to approaches that rely on early spectral collapse (e.g., PCA into 2D processing), which underutilize HSI. Trends are visualized in Figure 6 (right), quantitative references appear in Table 4.

### 5.3. Fusion Results

We compare BCAF against unimodal RGB/HSI baselines and a learned late-fusion baseline (logit fusion), all trained with identical backbones and schedules.

**Overall.** Across datasets, BCAF consistently improves mIoU and per-class IoU over the strongest unimodal RGB/HSI baselines and over the learned late-fusion baseline. On SpectralWaste, BCAF achieves state-of-the-art mIoU under the official split (see Table 2). On K3I-Material/Plastic, BCAF improves both taxonomies. Gains are larger for K3I-Material, where BCAF really benefits from the complementary cues of RGB and HSI, and smaller but consistent for Plastic-type, where unimodal HSI is already strong (see Tables 3 and 4).

**Why BCAF beats logit fusion.** Logit fusion aggregates decisions but lacks feature-level interactions. In contrast, BCAF performs bidirectional, local cross-attention between fine-grid RGB and coarse spectral slices, followed by gated fusion that modulates HSI contributions per channel and stage. This yields systemat-

ically higher, more stable gains than decision-level fusion at the same input sizes. On K3I-Plastic, where the mIoU gap between RGB and HSI is large (25 percentage points), logit fusion with unfrozen backbones allowed the weaker RGB stream to degrade strong HSI predictions, producing lower mIoU than HSI alone.

**SpectralWaste: HSI-1 vs. HSI-5 in fusion.** A central observation is that multi-slice HSI improves modality fusion even if the unimodal HSI-1 pipeline (spectral collapse, 2D processing) has a higher mIoU. With BCAF, RGB-1024+HSI-5 outperforms RGB-1024+HSI-1, because processing the  $k = 5$  slices contribute more complementary information to RGB. This can also be seen in the Oracle fusion, selecting, at each pixel, the correct prediction from RGB or HSI using ground truth (an upper bound on feature-level fusion without labels at test time). Here larger per-pixel lift over RGB can be seen HSI-5 than for HSI-1 (Figure 7), indicating less redundancy and richer spectral cues. This complementarity yields the best semantic segmentation with RGB-1024+HSI-5 (Table 2).

### 5.4. Computation Analysis

We assess inference efficiency and complexity via throughput (images/s), parameters, and theoretical GFLOPs, using the protocol described in Section 4.4. Summary values appear in Table 2.

**RGB scaling.** As input size increases, GFLOPs grow quadratically while parameters remain constant. From 256  $\rightarrow$  512, throughput is nearly unchanged (GPU underutilization at small sizes dominates). From 512  $\rightarrow$  1024, throughput drops noticeably, and 2048 is compute-heavy with a further decrease. Combined with

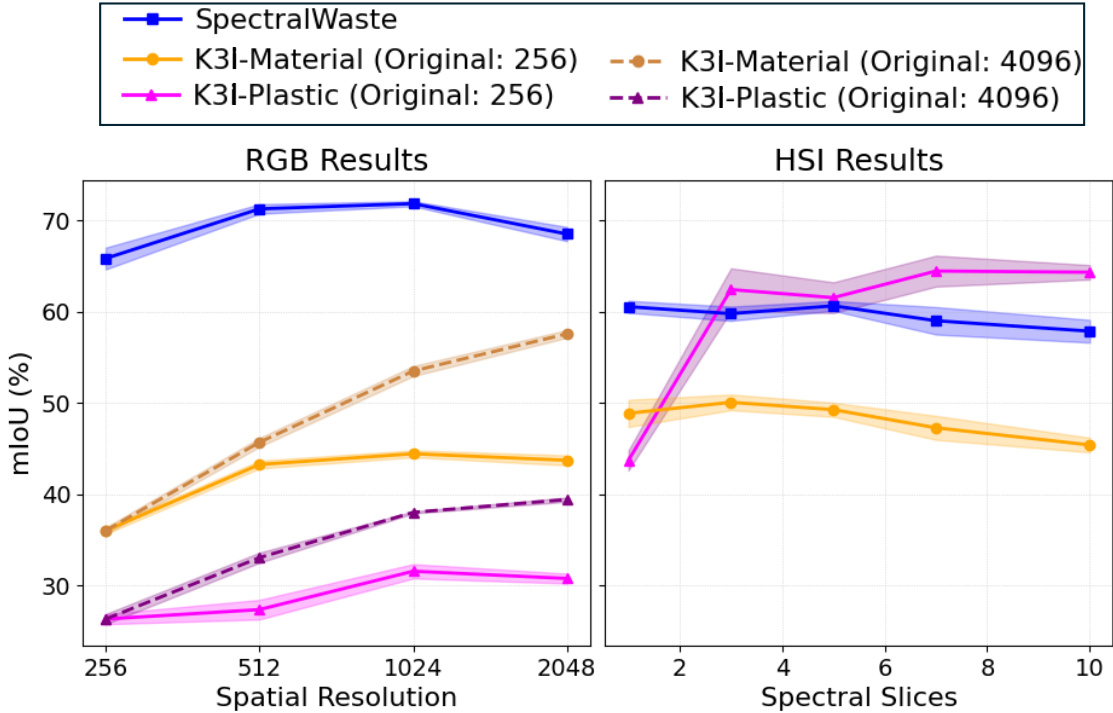


Figure 6: Effect of input resolution (left, RGB) and spectral slice count  $K$  (right, HSI) on segmentation performance across SpectralWaste and K3I-Material/Plastic. Curves summarize the trends of Sections 5.1 and 5.2. Higher mIoU is better.

the accuracy trends, 512 yields an almost “free” boost in accuracy, and 1024 offers a balanced operating point.

**HSI scaling.** Increasing the spectral slice count  $K$  adds approximately linear compute due to spectral self-attention. Throughput remains nearly flat up to small/intermediate  $K$  (e.g.,  $K \leq 5$ ) and declines for larger  $K$  (e.g., 7-10) as spectral attention begins to dominate latency.

**Fusion overhead (BCAF).** BCAF computes cross-attention locally at each coarse HSI location, so that  $r^2$  fine-grid RGB “children” interact with  $K$  spectral slices. This leads to a score-computation cost per stage that scales as  $\mathcal{O}(H_c W_c r^2 K)$ , rather than  $\mathcal{O}(r^2 K (H_c W_c)^2)$  for global all-to-all attention. In practice, the RGB and HSI backbones run efficiently in parallel, so the fusion overhead is modest. With RGB at 512 and  $K=5$  HSI slices, BCAF maintains real-time throughput while improving accuracy. Increasing RGB to 1024 with  $K=5$  reduces throughput as expected but remains viable for relaxed-latency settings.

### 5.5. Ablation Study

We ablate key components of the BCAF to validate design choices and quantify their impact under con-

trolled settings. All runs share identical data preprocessing, augmentations, optimization as in Section 4.2.

We first ablate the HSI backbone in a unimodal setting on SpectralWaste at  $256 \times 256$  with  $K=5$  slices to isolate spectral design choices. We probe three questions: (i) how to embed raw bands into  $K$  spectral slices (embedding), (ii) how to model spectral relations in the backbone (attention vs. convolution), and (iii) how to reduce the slice axis before the shared 2D decoder (spectral reduction). Results are in Table 5.

We then ablate fusion stage activation and directionality (RGB→HSI, HSI→RGB, bidirectional) and modality misalignment. We use RGB= 1024 and HSI=5 on SpectralWaste, and additionally report K3I-Material/Plastic results with RGB= 1024 and  $K=3$  and  $K=7$  respectively. Results are shown in Tables 6 and 7.

**HSI backbone: embedding.** Our baseline (grouped shared-kernel) preserves spectral structure by grouping contiguous bands ( $R_G=45$ ) and applying a single shared  $4 \times 4 \times R_G \rightarrow C$  convolution per group, yielding  $K$ -slices. We compare (1) a single large projection that uses one  $4 \times 4 \times S$  projection over all 224 bands to directly produce  $K=5$  tokens per location (no grouping, no weight sharing), (2) unshared per-group kernels with the same

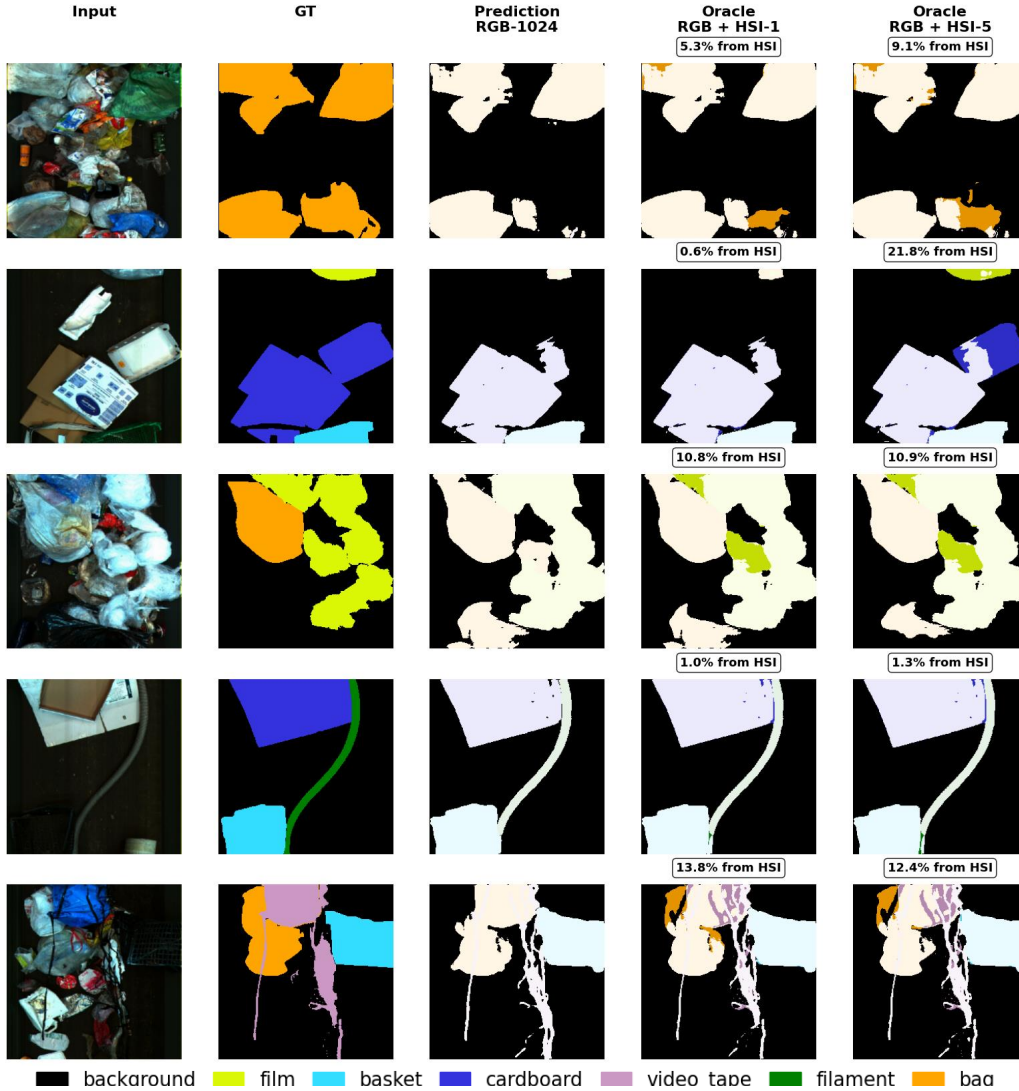


Figure 7: SpectralWaste: comparison of HSI-1 ( $K=1$ , spectral collapse) and HSI-5 ( $K=5$ , multi-slice). Oracle fusion (per-pixel best-of-modality using ground truth) shows a larger lift over RGB-1024 for HSI-5, evidencing stronger complementarity to RGB.

grouping but separate  $4 \times 4 \times R_G$  kernels per group (no sharing), (3) PCA-5 that collapses  $224 \rightarrow 5$  components globally before a  $4 \times 4 \times 1$  patch-embed per component, and (4) SavGol + PCA-5 that applies Savitzky-Golay smoothing [29] prior to PCA.

We find that preserving spectral locality with shared weights provides the best accuracy. In contrast, the single large projection and unshared per-group variants do not improve accuracy, while PCA-based variants consistently underperform, indicating that early spectral collapse discards discriminative narrowband structure needed downstream.

**HSI backbone: spectral modeling.** At each spa-

tial location, the baseline applies position-wise spectral self-attention over the  $K$  slices with learnable spectral positional encodings (content-adaptive mixing). We replace this with a 1D Conv along the slice axis (fixed local spectral receptive field) to test whether explicit attention is necessary. Replacing attention with 1D convolution yields a mIoU drop, suggesting that fixed kernels underfit slice correlations and cannot adapt mixing to class- and instance-specific spectral patterns.

**HSI backbone: spectral reducer (pre-decoder).**

Before the shared 2D decoder, the baseline spectral SE performs input-adaptive per-slice and per-channel gating followed by a weighted sum over  $K$  (Section 3.4).

Table 5: HSI (unimodal) ablations on SpectralWaste: embedding variants, spectral modeling, and spectral reducer. All use  $K=5$  unless noted.  $\Delta$  is measured against the baseline row within each block.

Block	Variant	mIoU (%) $\uparrow$	Img./s $\uparrow$	Params (M) $\downarrow$	GFLOPs $\downarrow$
<i>Embedding variants</i>	Grouped shared-kernel (baseline)	<b>60.3 <math>\pm</math> 0.9</b>	118.8	45.417	54.343
	Single large projection	56.7 $\pm$ 1.5	117.9	47.076	60.005
	Unshared per-group kernels	56.1 $\pm$ 2.5	120.4	45.694	54.343
	PCA-5	57.6 $\pm$ 1.6	123.1	45.356	52.959
	SavGol + PCA-5	53.9 $\pm$ 1.5	123.5	45.356	52.959
<i>Spectral modeling in backbone</i>	Spectral attention (baseline)	<b>60.3 <math>\pm</math> 0.9</b>	118.8	45.417	54.343
	1D Conv	58.1 $\pm$ 1.1	131.1	41.084	49.790
<i>Spectral reducer before decoder</i>	Spectral SE (baseline)	<b>60.3 <math>\pm</math> 0.9</b>	118.8	45.417	54.343
	Learnable Weighted Reducer	60.0 $\pm$ 0.8	121.3	45.220	54.342

We compare a learnable weighted reducer that uses a global, input-independent vector of  $K$  weights (shared across all channels). Spectral SE yields slightly higher mIoU, indicating that conditioning the spectral slice weights on features improves robustness to noise and class-dependent spectral variability at negligible overhead.

**Fusion: BCAF stage-wise effect.** Table 6 ablates the fusion stage and directionality. All-stage, bidirectional cross-attention performs best, confirming the value of multi-scale, localized interactions between high-resolution RGB and coarser multi-slice HSI. Fusing only at the last stage (with RGB used via the head skip connection elsewhere) is close on SpectralWaste but lags on K3I-Cycling. Especially mIoU drops on K3I-Plastic, suggesting that early-stage cues aid alignment in more diverse scenes. Fusing only at the first stage consistently reduces mIoU. Unidirectional variants underperform bidirectional.

**Fusion: Modality misalignment.** We assess robustness to cross-modal registration errors by shifting HSI only while keeping RGB and labels fixed. All models are trained on aligned data, results can be seen in Table 7). Across datasets, BCAF is more robust than late logit fusion for small-to-moderate shifts, indicating that localized, multi-scale cross-attention buffers modest misregistrations. The degradation pattern mirrors modality information content: SpectralWaste changes little under HSI shifts (RGB-dominated), K3I-Material degrades moderately (balanced cues), and K3I-Plastic is most sensitive (HSI-dominated). At extreme shifts, when cross-modal overlap largely disappears, fusion benefits diminish and the gap to late fusion narrows.

**Fusion: Training protocol.** Initializing BCAF’s RGB and HSI backbones from the best unimodal checkpoints, then fine-tuning the full fusion model end-to-end, yields more stable convergence and higher mIoU than starting from ImageNet-initialized back-

bones (55.9  $\pm$  1.8 on SpectralWaste), with no architectural changes.

## 6. Conclusion

We addressed pixel-accurate, real-time waste sorting by fusing high-resolution RGB with lower-resolution HSI without collapsing spectra or eroding spatial detail. We introduced Bidirectional Cross-Attention Fusion (BCAF), which (i) adapts Swin Transformer to HSI via grouped spectral tokenization and factorized spatial-spectral attention, (ii) aligns fine-grid RGB and coarse-grid HSI features through localized, bidirectional cross-attention across multiple scales, and (iii) employs spectral SE pooling and gated fusion to share a single, lightweight decoder across RGB, HSI, and fused inputs.

Across SpectralWaste and our industrial K3I-Cycling datasets, three trends stand out. (1) Scaling the RGB input improves segmentation, and the biggest gains appear when larger inputs preserve native high-resolution detail. (2) Preserving and attending along the spectral axis in our adapted HSI backbone provides genuinely complementary cues beyond 2D backbones and it clearly excels when spectral signatures dominate (e.g., plastic-type discrimination). (3) Building on these strengths, BCAF couples fine-grid RGB structure with multi-slice HSI features via localized, bidirectional cross-attention, consistently surpassing unimodal baselines and learned logit-level fusion and achieving state-of-the-art performance on SpectralWaste at practical throughput.

A limitation is that the method assumes paired, well-registered acquisition: localized multi-scale cross-attention tolerates small shifts, but severe spatial/temporal misregistration degrades fusion. The dual-backbone design increases parameters and compute. Performance is sensitive to the HSI slice count  $K$ : small  $K$  can underuse spectral detail on fine-grained

Table 6: Fusion ablations (RGB 1024). Bidirectional refers to both RGB→HSI and HSI→RGB within each fusion block.

Config	Stages	Direction	SpectralWaste mIoU (%)	K3I-Material mIoU (%)	K3I-Plastic mIoU (%)	Img/s ↑	Params (M) ↓	GFLOPs ↓
Early only	1	bidirectional	73.2 ± 0.3	59.5 ± 0.8	59.1 ± 1.1	35.4	82.477	228.937
Late only	4	bidirectional	76.3 ± 0.5	58.9 ± 0.7	61.9 ± 1.5	38.6	96.579	225.979
All stages	1-4	bidirectional	<b>76.4 ± 0.4</b>	<b>61.8 ± 1.2</b>	<b>66.2 ± 1.7</b>	31.4	101.296	282.176
All stages	1-4	RGB→HSI	76.0 ± 0.6	60.4 ± 1.5	61.5 ± 0.7	32.6	98.156	228.908
All stages	1-4	HSI→RGB	76.3 ± 0.3	60.4 ± 0.8	60.3 ± 1.5	33.1	98.156	268.166

Table 7: Absolute mIoU (%) under HSI-only spatial shifts (pixels on the HSI grid). RGB and labels remain fixed, while HSI is shifted by  $(dx, dy)$  with zero padding. All models are trained on aligned data.

Model / Dataset	(0,0) mIoU	(2,2)	(4,4)	(8,8)	(16,16)	(32,32)	(64,64)
Logit fusion (SpectralWaste)	72.6 ± 0.8	72.7 ± 0.8	72.6 ± 0.8	72.2 ± 0.6	69.5 ± 1.2	58.8 ± 2.7	36.2 ± 4.9
BCAF (SpectralWaste)	76.4 ± 0.4	76.3 ± 0.5	76.3 ± 0.4	76.0 ± 0.3	75.3 ± 0.4	73.4 ± 0.6	69.1 ± 1.3
Logit fusion (K3I-Material)	57.9 ± 0.2	57.5 ± 0.4	55.8 ± 0.8	50.7 ± 1.3	42.7 ± 1.2	37.4 ± 1.4	36.6 ± 1.1
BCAF (K3I-Material)	62.3 ± 1.1	62.2 ± 1.2	61.1 ± 1.3	57.9 ± 1.2	50.6 ± 1.3	45.0 ± 1.41	44.8 ± 1.4
Logit fusion (K3I-Plastic)	58.0 ± 4.5	57.6 ± 4.6	55.6 ± 4.2	49.6 ± 2.0	38.3 ± 1.3	26.2 ± 3.7	21.2 ± 4.2
BCAF (K3I-Plastic)	66.2 ± 1.7	66.0 ± 1.8	63.8 ± 1.8	58.0 ± 2.0	45.0 ± 1.1	27.0 ± 1.0	18.5 ± 1.5

tasks, whereas large  $K$  improves discrimination at added latency and potential noise ( $K$  should be tuned per task). Finally, the approach presumes synchronized sensors and calibration, which may limit deployment where reliable pairing is unavailable.

Future work includes extending BCAF to other co-registered RGB+X sensing modalities (e.g., multispectral, NIR/SWIR, thermal, depth/ToF). We also plan to deploy it on a real conveyor system to assess end-to-end performance under realistic operating conditions. In addition, given the abundance of unlabeled HSI data and the lack of established hyperspectral foundation models, we plan to investigate self-supervised pre-training strategies for the HSI backbone, analogous to how ImageNet pretraining benefits the RGB backbone, with the aim of further improving robustness and segmentation accuracy.

In summary, BCAF preserves hyperspectral structure and aligns it with high-resolution RGB through multi-scale, bidirectional cross-attention, delivering accurate and efficient multimodal segmentation.

## Acknowledgement

We would like to thank Steffen Ruger and his team of the Fraunhofer Institute for Integrated Circuits IIS for their support in dataset annotation. We also thank Lobbe RSW GmbH (Iserlohn, Germany) for providing samples of lightweight packaging waste.

## Data availability

SpectralWaste: Publicly available at <https://github.com/ferpb/spectralwaste-dataset>

[10]. We used the dataset under the terms of the original repository.

K3I-Cycling: Proprietary dataset collected at Fraunhofer IOSB with support from Lobbe RSW GmbH. Not fully publicly released yet. First subset already available at <http://dx.doi.org/10.24406/fordatis/420>.

## Code availability

We will release the full source code for BCAF, including training and evaluation scripts, configuration files, and pretrained checkpoints, upon acceptance.

## Funding

Funding was provided by the Federal Ministry of Research, Technology and Space (BMFTR) under the funding reference 033KI201.

## Declaration of competing interest

The authors declare no competing financial or non-financial interests.

## Declaration of generative AI and AI-assisted technologies in the writing process

During the preparation of this work the authors used FhGenie (GPT5-based) in order to improve readability. After using this tool, the authors reviewed and edited the content as needed and take full responsibility for the content of the publication.

## References

- [1] G. Maier, R. Gruna, T. Längle, J. Beyerer, A survey of the state of the art in sensor-based sorting technology and research, *IEEE Access* 12 (2024).
- [2] C. Chang, *Hyperspectral Imaging: Techniques for Spectral Detection and Classification*, Springer Science & Business Media, 2003.
- [3] D. A. Burns, E. W. Ciurczak (Eds.), *Handbook of Near-Infrared Analysis*, 3rd Edition, CRC Press, 2007.
- [4] J. Zhang, H. Liu, K. Yang, X. Hu, R. Liu, R. Stiefelwagen, Cmx: Cross-modal fusion for rgb-x semantic segmentation with transformers, *IEEE Transactions on intelligent transportation systems* 24 (12) (2023) 14679–14694.
- [5] H. Zhou, L. Qi, H. Huang, X. Yang, Z. Wan, X. Wen, Canet: Co-attention network for rgb-d semantic segmentation, *Pattern Recognition* 124 (2022) 108468.
- [6] Y. Li, X. Zhang, Hybrid long-range feature fusion network for multi-modal waste semantic segmentation, *Information Fusion* (2025) 103608.
- [7] M. Bihler, L. Roming, Y. Jiang, A. J. Afifi, J. Aderhold, D. Čibiraitė-Lukenskienė, S. Lorenz, R. Gloaguen, R. Gruna, M. Heizmann, Multi-sensor data fusion using deep learning for bulky waste image classification, in: *Automated Visual Inspection and Machine Vision V*, Vol. 12623, SPIE, 2023, pp. 69–82.
- [8] Z. Liu, Y. Lin, Y. Cao, H. Hu, Y. Wei, Z. Zhang, S. Lin, B. Guo, Swin transformer: Hierarchical vision transformer using shifted windows, *CoRR abs/2103.14030* (2021).
- [9] O. Ronneberger, P. Fischer, T. Brox, U-net: Convolutional networks for biomedical image segmentation, in: *Medical Image Computing and Computer-Assisted Intervention (MICCAI)*, Vol. 9351, 2015.
- [10] S. Casao, F. Peña, A. Sabater, R. Castellón, D. Suárez, E. Montijano, A. C. Murillo, Spectral-waste dataset: Multimodal data for waste sorting automation, in: *2024 IEEE/RSJ International Conference on Intelligent Robots and Systems (IROS)*, IEEE, 2024, pp. 5852–5858.
- [11] European Parliament, How to reduce plastic waste: Eu measures explained, <https://www.europarl.europa.eu/topics/en/article/20180830ST011347/how-to-reduce-plastic-waste-eu-measures-explained#plastic-packaging-waste-10>, accessed: 10 Dec 2025.
- [12] A. Paszke, A. Chaurasia, S. Kim, E. Culurciello, Enet: A deep neural network architecture for real-time semantic segmentation, arXiv preprint arXiv:1606.02147 (2016).
- [13] H. Zhao, X. Qi, X. Shen, J. Shi, J. Jia, Icn-net for real-time semantic segmentation on high-resolution images, in: *Proceedings of the European conference on computer vision (ECCV)*, 2018, pp. 405–420.
- [14] E. Xie, W. Wang, Z. Yu, A. Anandkumar, J. M. Álvarez, P. Luo, Segformer: Simple and efficient design for semantic segmentation with transformers, *CoRR* (2021).
- [15] A. Senanayake, M. Arashpour, Automated electro-construction waste sorting: Computer vision for part-level segmentation, *Waste Management* 203 (2025) 114883.
- [16] M. Ahmad, S. Distefano, A. M. Khan, M. Mazzara, C. Li, H. Li, J. Aryal, Y. Ding, G. Vivone, D. Hong, A comprehensive survey for hyperspectral image classification: The evolution from conventional to transformers and mamba models, *Neurocomputing* 644 (2025).
- [17] D. Hong, Z. Han, J. Yao, L. Gao, B. Zhang, A. Plaza, J. Chanussot, Spectralformer: Rethinking hyperspectral image classification with transformers, *CoRR* (2021).
- [18] A. Dosovitskiy, L. Beyer, A. Kolesnikov, D. Weissenborn, X. Zhai, T. Unterthiner, M. Dehghani, M. Minderer, G. Heigold, S. Gelly, J. Uszkoreit, N. Houlsby, An image is worth 16x16 words: Transformers for image recognition at scale, *International Conference on Learning Representations* (2021).
- [19] X. Yang, W. Cao, Y. Lu, Y. Zhou, Hyperspectral image transformer classification networks, *IEEE Transactions on Geoscience and Remote Sensing* 60 (2022).

- [20] X. He, Y. Chen, Z. Lin, Spatial-spectral transformer for hyperspectral image classification, *Remote Sensing* 13 (3) (2021).
- [21] L. Sun, G. Zhao, Y. Zheng, Z. Wu, Spectral-spatial feature tokenization transformer for hyperspectral image classification, *IEEE Transactions on Geoscience and Remote Sensing* 60 (2022).
- [22] J. Long, E. Shelhamer, T. Darrell, Fully convolutional networks for semantic segmentation, in: *Proceedings of the IEEE conference on computer vision and pattern recognition*, 2015, pp. 3431–3440.
- [23] L.-C. Chen, G. Papandreou, I. Kokkinos, K. Murphy, A. L. Yuille, Deeplab: Semantic image segmentation with deep convolutional nets, atrous convolution, and fully connected crfs, *IEEE transactions on pattern analysis and machine intelligence* 40 (4) (2017) 834–848.
- [24] T. Ji, H. Fang, R. Zhang, J. Yang, Z. Wang, X. Wang, Plastic waste identification based on multimodal feature selection and cross-modal swin transformer, *Waste Management* 192 (2025).
- [25] M. Ali, O. A. AlSuwaidi, Fusionsort: Enhanced cluttered waste segmentation with advanced decoding and comprehensive modality optimization, *arXiv preprint arXiv:2508.19798* (2025).
- [26] J. Hu, L. Shen, G. Sun, Squeeze-and-excitation networks, in: *Proceedings of the IEEE conference on computer vision and pattern recognition*, 2018, pp. 7132–7141.
- [27] W. Shi, J. Caballero, F. Huszár, J. Totz, A. P. Aitken, R. Bishop, D. Rueckert, Z. Wang, Real-time single image and video super-resolution using an efficient sub-pixel convolutional neural network, in: *Proceedings of the IEEE conference on computer vision and pattern recognition*, 2016, pp. 1874–1883.
- [28] R. Wightman, Pytorch image models, <https://github.com/rwightman/pytorch-image-models> (2019). doi: 10.5281/zenodo.4414861.
- [29] R. W. Schafer, What is a savitzky-golay filter?, *IEEE Signal Processing Magazine* 28 (4) (2011) 111–117.

## Appendix

### *Dataset Class Spectra*

We show the mean normalized spectra for each class in all datasets. First, the HSI data is normalized. Then, for each class, all corresponding pixels are aggregated and the mean spectrum over channels is computed and plotted (see Figure 8).

### *Semantic segmentation on K3I-Material*

Additional qualitative segmentation results on K3I-Material. We compare Swin-T RGB at 1024 and 2048, adapted Swin-T HSI with  $K=3$  spectral slices, and BCAF (RGB-1024 + HSI-3). Relative to Spectral-Waste (RGB at  $256 \times 256$ ), the native-resolution regime on K3I-Material yields clear gains: downsampling from the  $4096 \times 4096$  acquisition to 2048 improves performance, whereas pure upscaling from  $256 \times 256$  degrades. BCAF improvements are especially visible for the paper/cardboard class. These observations align with the quantitative gains in Section 5.

### *Visualization of Swin-T backbone feature activations*

We visualize Swin-T backbone activations across stages for input resolutions 256 vs 1024 by computing per-stage heatmaps. For each stage output  $\mathbf{F}_{\text{rgb}} \in \mathbb{R}^{H \times W \times C}$ , we average over channels to obtain a single spatial map  $\mathbf{A} = \text{mean}_c(\mathbf{F}_{\text{rgb}}) \in \mathbb{R}^{H \times W}$ . We apply min-max normalization to  $[0,1]$  and render with a magma colormap.

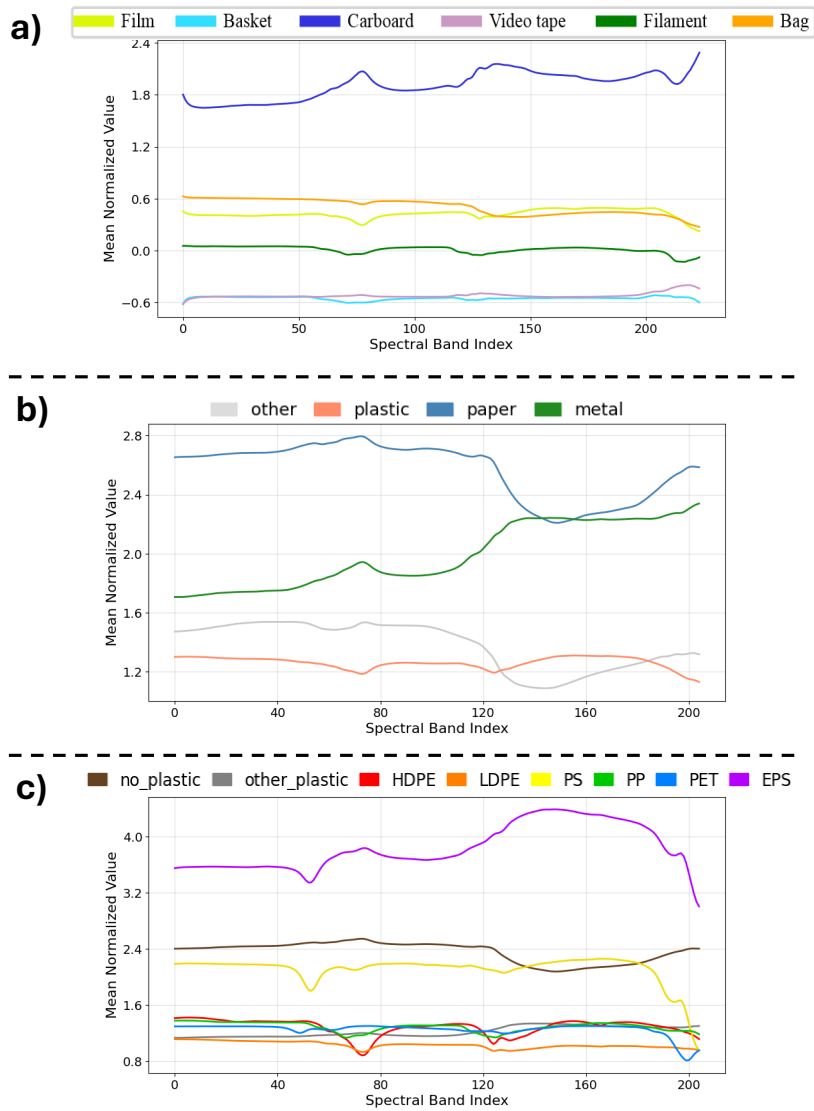


Figure 8: Mean normalized spectra per class for (a) SpectralWaste, (b) K3I-Material, and (c) K3I-Plastic.

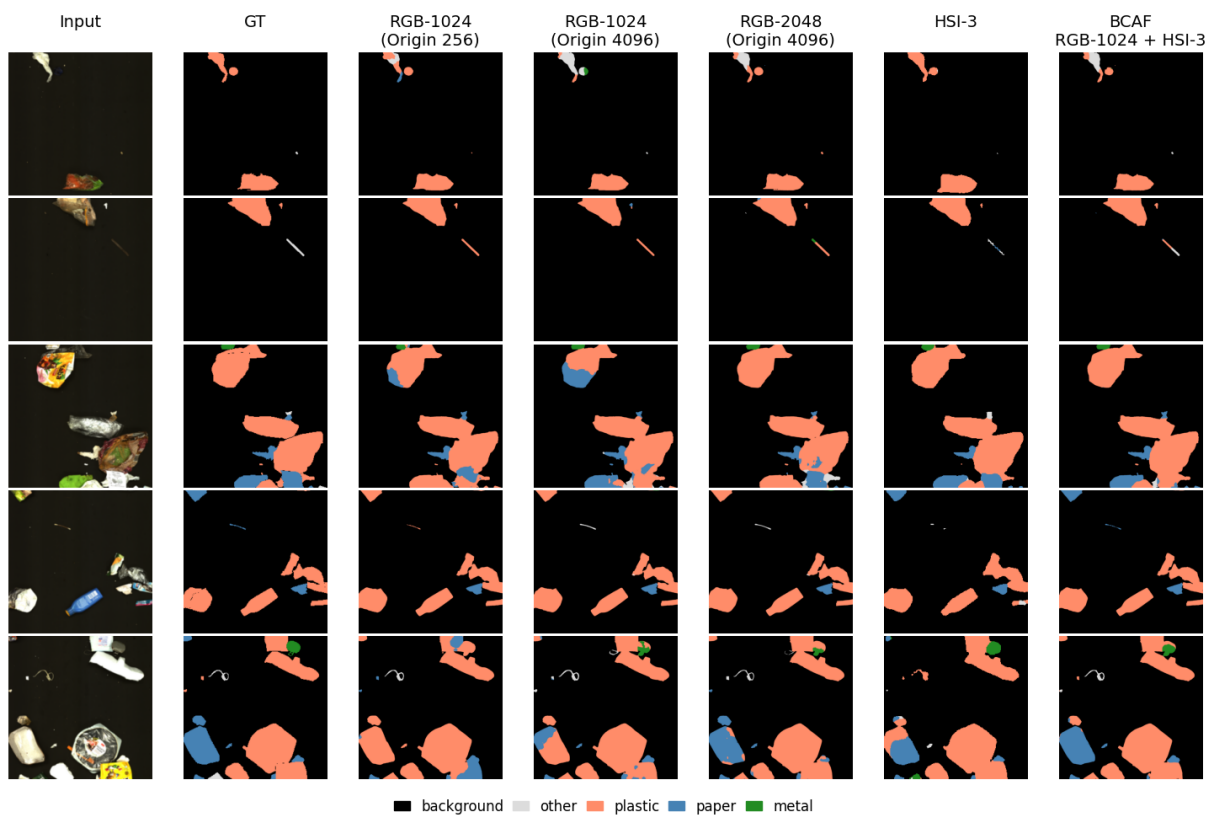


Figure 9: K3I-Material qualitative results. Shown are Swin-T RGB at 1024 and 2048, adapted Swin-T HSI-3, and BCAF (RGB 1024 + HSI-3).

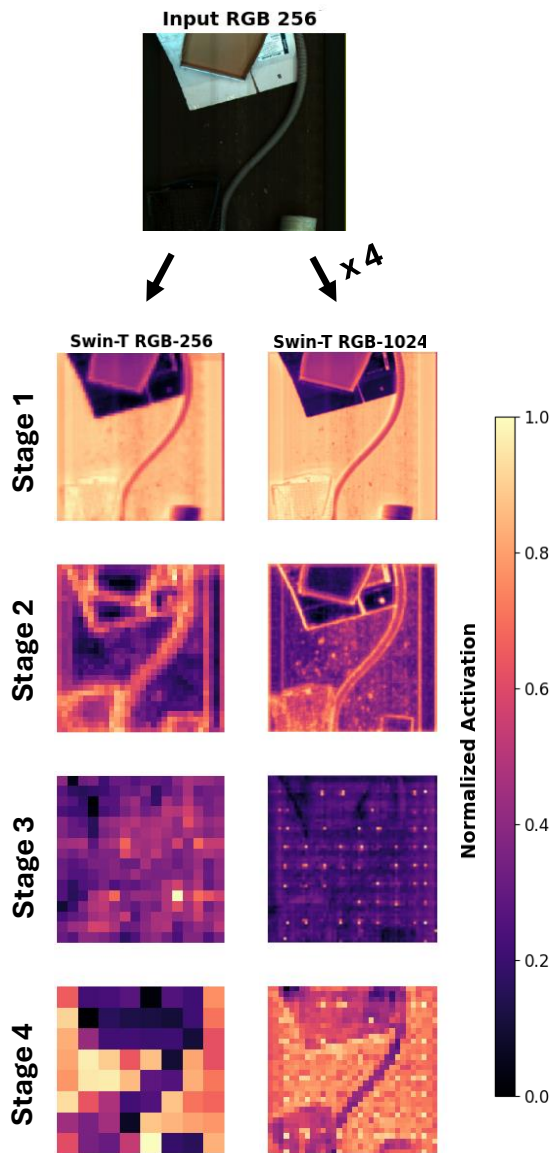


Figure 10: Swin-T feature activations across stages for input resolutions 256 vs 1024. Activations are mean over channels, normalized to [0,1].